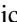






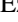
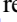













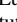
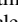
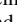
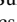




BAT AGN Spectroscopic Survey. XX. Molecular Gas in Nearby Hard-X-Ray-selected AGN Galaxies

Michael J. Koss¹ , Benjamin Strittmatter² , Isabella Lamperti³ , Taro Shimizu⁴ , Benny Trakhtenbrot⁵ ,
 Amelie Saintonge³ , Ezequiel Treister⁶ , Claudia Cicone⁷ , Richard Mushotzky⁸ , Kyuseok Oh^{9,10,29} ,
 Claudio Ricci^{11,12,13} , Daniel Stern¹⁴ , Tonima Tasnim Ananna¹⁵ , Franz E. Bauer^{16,17,18} , George C. Privon¹⁹ ,
 Rudolf E. Bär² , Carlos De Breuck²⁰ , Fiona Harrison²¹ , Kohei Ichikawa²² , Meredith C. Powell²³ , David Rosario²⁴ ,
 David B. Sanders²⁵ , Kevin Schawinski²⁶ , Li Shao²⁷ , C. Megan Urry²⁸ , and Sylvain Veilleux⁸ 

¹Eureka Scientific, 2452 Delmer Street, Suite 100, Oakland, CA 94602-3017, USA; mike.koss@eurekasci.com

²Institute for Particle Physics and Astrophysics, ETH Zürich, Wolfgang-Pauli-Strasse 27, CH-8093 Zürich, Switzerland

³Department of Physics and Astronomy, University College London, Gower Street, London WC1E 6BT, UK

⁴Max-Planck-Institut für extraterrestrische Physik, Postfach 1312, D-85741 Garching, Germany

⁵School of Physics and Astronomy, Tel Aviv University, Tel Aviv 69978, Israel

⁶Instituto de Astrofísica, Facultad de Física, Pontificia Universidad Católica de Chile, Casilla 306, Santiago 22, Chile

⁷Institute of Theoretical Astrophysics, University of Oslo, Postboks 1029, Blindern No-0315 Oslo, Norway

⁸Department of Astronomy, University of Maryland, College Park, MD 20742, USA

⁹Korea Astronomy & Space Science Institute, 776, Daedeokdae-ro, Yuseong-gu, Daejeon 34055, Republic of Korea

¹⁰Department of Astronomy, Kyoto University, Kitashirakawa-Oiwake-cho, Sakyo-ku, Kyoto 606-8502, Japan

¹¹Núcleo de Astronomía de la Facultad de Ingeniería, Universidad Diego Portales, Av. Ejército Libertador 441, Santiago 22, Chile

¹²Kavli Institute for Astronomy and Astrophysics, Peking University, Beijing 100871, People's Republic of China

¹³George Mason University, Department of Physics & Astronomy, MS 3F3, 4400 University Drive, Fairfax, VA 22030, USA

¹⁴Jet Propulsion Laboratory, California Institute of Technology, 4800 Oak Grove Drive, MS 169-224, Pasadena, CA 91109, USA

¹⁵Department of Physics & Astronomy, Dartmouth College, 6127 Wilder Laboratory, Hanover, NH 03755, USA

¹⁶Instituto de Astrofísica and Centro de Astroingeniería, Facultad de Física, Pontificia Universidad Católica de Chile, Casilla 306, Santiago 22, Chile

¹⁷Millennium Institute of Astrophysics (MAS), Nuncio Monseñor Sótero Sanz 100, Providencia, Santiago, Chile

¹⁸Space Science Institute, 4750 Walnut Street, Suite 205, Boulder, CO 80301, USA

¹⁹Department of Astronomy, University of Florida, 211 Bryant Space Science Center, Gainesville, FL 32611, USA

²⁰European Southern Observatory, Karl Schwarzschild Str 2, D-85748 Garching, Germany

²¹Cahill Center for Astronomy and Astrophysics, California Institute of Technology, Pasadena, CA 91125, USA

²²Frontier Research Institute for Interdisciplinary Sciences, Tohoku University, Sendai 980-8578, Japan

²³Institute of Particle Astrophysics and Cosmology, Stanford University, 452 Lomita Mall, Stanford, CA 94305, USA

²⁴Centre for Extragalactic Astronomy, Department of Physics, Durham University, South Road, DH1 3LE Durham, UK

²⁵Institute for Astronomy, 2680 Woodlawn Drive, University of Hawaii, Honolulu, HI 96822, USA

²⁶Modulus AG, Technoparkstrasse 1, CH-8005 Zurich, Switzerland

²⁷National Astronomical Observatories, Chinese Academy of Sciences, 20A Datun Road, Chaoyang District, Beijing 100012, People's Republic of China

²⁸Yale Center for Astronomy & Astrophysics, Physics Department, New Haven, CT 06520, USA

Received 2020 February 21; revised 2020 October 10; accepted 2020 October 19; published 2021 February 4

Abstract

We present the host-galaxy molecular gas properties of a sample of 213 nearby ($0.01 < z < 0.05$) hard-X-ray-selected active galactic nucleus (AGN) galaxies, drawn from the 70-month catalog of Swift's Burst Alert Telescope (BAT), with 200 new CO(2–1) line measurements obtained with the James Clerk Maxwell Telescope and the Atacama Pathfinder Experiment telescope. We find that AGN in massive galaxies ($\log(M_*/M_\odot) > 10.5$) tend to have more molecular gas and higher gas fractions than inactive galaxies matched in stellar mass. When matched in star formation, we find AGN galaxies show no difference from inactive galaxies, with no evidence that AGN feedback affects the molecular gas. The higher molecular gas content is related to AGN galaxies hosting a population of gas-rich early types with an order of magnitude more molecular gas and a smaller fraction of quenched, passive galaxies ($\sim 5\%$ versus 49%) compared to inactive galaxies. The likelihood of a given galaxy hosting an AGN ($L_{\text{bol}} > 10^{44} \text{ erg s}^{-1}$) increases by ~ 10 – 100 between a molecular gas mass of $10^{8.7} M_\odot$ and $10^{10.2} M_\odot$. AGN galaxies with a higher Eddington ratio ($\log(L/L_{\text{Edd}}) > -1.3$) tend to have higher molecular gas masses and gas fractions. The $\log(N_{\text{H}}/\text{cm}^{-2}) > 23.4$ of AGN galaxies with higher column densities are associated with lower depletion timescales and may prefer hosts with more gas centrally concentrated in the bulge that may be more prone to quenching than galaxy-wide molecular gas. The significant average link of host-galaxy molecular gas supply to supermassive black hole (SMBH) growth may naturally lead to the general correlations found between SMBHs and their host galaxies, such as the correlations between SMBH mass and bulge properties, and the redshift evolution of star formation and SMBH growth.

Unified Astronomy Thesaurus concepts: Active galactic nuclei (16); AGN host galaxies (2017); Molecular gas (1073); Surveys (1671); X-ray active galactic nuclei (2035); Survival analysis (1905); Submillimeter astronomy (1647); High energy astrophysics (739); Seyfert galaxies (1447); Catalogs (205)

Supporting material: figure set, machine-readable tables

²⁹ JSPS Fellow.

1. Introduction

The study of cold molecular gas and its properties in galaxies hosting active galactic nuclei (AGNs) is crucial for understanding the growth of supermassive black holes (SMBHs) and how they affect their host galaxies. There appears to be an evolutionary link between the merger of gas-rich spirals, ultraluminous infrared (IR) galaxies, and luminous quasars (e.g., Sanders et al. 1988; Hopkins et al. 2008; Veilleux et al. 2009). However, our understanding of this evolution and AGN fueling is biased by the IR preselection, as most CO surveys have focused on far-IR (FIR) bright AGN (Rigopoulou et al. 1997; Monje et al. 2011; Kirkpatrick et al. 2019) to ensure a large number of detections.

Early studies surveyed optically selected Seyferts in the accessible $^{12}\text{CO } J = 1-0$ transition³⁰ (Heckman et al. 1989; Maiolino & Rieke 1995). Some surveys have focused on X-ray-selected FIR-bright AGN (Yamada 1994; Monje et al. 2011). Some of these studies found that obscured AGN that lack broad Balmer lines (i.e., Seyfert 2 AGN) have increased IR emission from their disk, suggesting the nuclear toroidal structure hypothesized to obscure the broad-line region in type 2 Seyferts (e.g., Antonucci 1993). However, other studies have found no difference (Maiolino et al. 1997).

Several observational studies have found that AGN host galaxies appear to lie in the “green valley” on the color-magnitude diagram, in between actively star-forming galaxies in the blue cloud and passively evolving galaxies on the red sequence (Silverman et al. 2008; Georgakakis et al. 2009; Schawinski et al. 2015). The lower star formation rates (SFRs) associated with the green valley AGN galaxies are attributed to AGN feedback where any reservoir of gas is either heated and/or expelled or simply not accreted (Schawinski et al. 2009; Pović et al. 2012; Cimatti et al. 2013; Mahoro et al. 2017). Recent interferometric observations, particularly with ALMA (see e.g., Combes 2018 for a review), have found many examples of molecular outflows in both low- and high-redshift AGN galaxies (e.g., Feruglio et al. 2010; Dasyra & Combes 2012; Brusa et al. 2018; Cicone et al. 2018; Alonso-Herrero et al. 2019; Bischetti et al. 2019; Fluetsch et al. 2019), though there are large uncertainties in the gas mass and other properties due to the assumptions and the limited samples considered. Thus, studying molecular gas in AGN hosts can provide a direct observational test for the presence or destruction of the molecular gas reservoir.

With the current sensitivity of large, single-dish millimeter-wavelength telescopes, larger ($N > 50$) surveys directed toward unbiased samples of star-forming galaxies and AGN galaxies (i.e., not FIR biased) are now possible. For nearby galaxies with extended structure, single-dish observations are better able to recover total extended CO emission than interferometers. Such surveys have included low-mass galaxies (ALLSMOG; Bothwell et al. 2014; Cicone et al. 2017) and late-type galaxies belonging to the Herschel Reference Survey (HRS; Boselli et al. 2014). The IRAM 30 m CO Legacy Database for the GALEX Arcicibo SDSS Survey (COLD GASS; Saintonge et al. 2011a, 2011b; Kauffmann et al. 2012) with 350 galaxies was one of the first large CO studies in the nearby universe whose sample was purely limited by stellar mass ($\log(M_*/M_\odot) > 10$). The survey was further extended to 532 galaxies in xCOLD GASS (Saintonge et al. 2017). The

survey has been used to trace the abundance of molecular gas in galaxies as a function of their mass, color, and morphology to understand the mechanisms that contribute to galaxy growth and quenching. The COLD GASS surveys were based on IRAM 30 m measurements and complementary Atacama Pathfinder Experiment (APEX) CO(2–1) observations, including both CO(1–0) and CO(2–1) line fluxes and offset pointings. This provides a robust CO luminosity function for inactive galaxies, well-calibrated CO(2–1)/CO(1–0) excitation corrections, and scaling relations between gas fraction (f_{H_2}), depletion timescales [$t_{\text{dep}}(\text{H}_2) \equiv M_{\text{H}_2}/\text{SFR}$], specific star formation rates ($\text{sSFR} \equiv \text{SFR}/M_*$), and global galaxy properties. Thus xCOLD GASS serves as an ideal reference comparison sample for studies of AGN host galaxies.

There are a handful of Seyferts in the xCOLD GASS sample, many of which appear to have large molecular gas reservoirs, but the statistics are too poor to understand the link to AGN host galaxies in detail. A study of (molecular and atomic) gas based on dust masses inferred from the FIR-submillimeter spectral energy distribution (SED) fitting of stacked samples of AGN galaxies at $z < 1$ found both higher gas mass and higher gas fractions in AGN hosts (Vito et al. 2014). Conversely, several small studies of powerful, distant AGN ($N = 3-15$, $z = 1-3$) hosts have found lower molecular gas fractions and depletion timescales (Fiore et al. 2017; Kakkad et al. 2017; Perna et al. 2018). A dedicated AGN galaxy survey, with comparatively large numbers ($N > 200$) to xCOLD GASS, is therefore needed to understand the average molecular gas and depletion timescales in nearby AGN galaxies.

The Burst Alert Telescope (BAT; Barthelmy et al. 2005) on board the Neil Gehrels Swift Observatory (Gehrels et al. 2004) has opened up a fundamentally new way to identify and study accreting SMBHs, as ultrahard X-rays (> 15 keV) can penetrate gas and dust to directly probe the central engine of the AGN. Ultrahard X-rays are therefore less biased by host-galaxy properties, which can strongly affect optical and IR techniques for finding AGN (e.g., Mateos et al. 2012; Ichikawa et al. 2017). In addition, the ultrahard X-rays are less affected by obscuration of the AGN, provided the material is thin to Compton scattering (i.e., $\log(N_{\text{H}}/\text{cm}^{-2}) \lesssim 24$; e.g., Ricci et al. 2015; Koss et al. 2016). The AGN detected with BAT are mainly nearby ($\langle z \rangle = 0.035$), which allows observers to obtain high signal-to-noise ratio (S/N) ancillary data for a large subset of these systems. Thus, studying BAT AGN galaxies allows for a high level of completeness, avoiding previously present biases related to FIR selection.

Previous studies have found that the morphologies and star formation characteristics of the host galaxies of ultrahard-X-ray-selected AGN galaxies differ significantly from inactive galaxies and from optically selected AGN galaxies. Ultrahard-X-ray-selected AGN appear to be predominantly hosted by rare, massive spirals or mergers (Koss et al. 2010, 2011a). At high stellar masses ($\log(M_*/M_\odot) > 10.5$) these AGN are $\sim 10-100$ times more likely to be in spiral hosts than inactive galaxies or optically selected AGN, which are hosted almost exclusively in red ellipticals. BAT AGN galaxies are significantly more FIR luminous than inactive galaxies or optical Seyferts at the same redshift ($0.01 < z < 0.05$), as the majority of BAT AGN (54%) galaxies are detected with Akari at $90 \mu\text{m}$, compared to only 4% of optically selected AGN galaxies (i.e., emission-line selection) and only 5% of inactive galaxies in the Sloan Digital Sky Survey (SDSS; Koss et al. 2011a).

³⁰ Hereafter, we simply refer to ^{12}CO as CO.

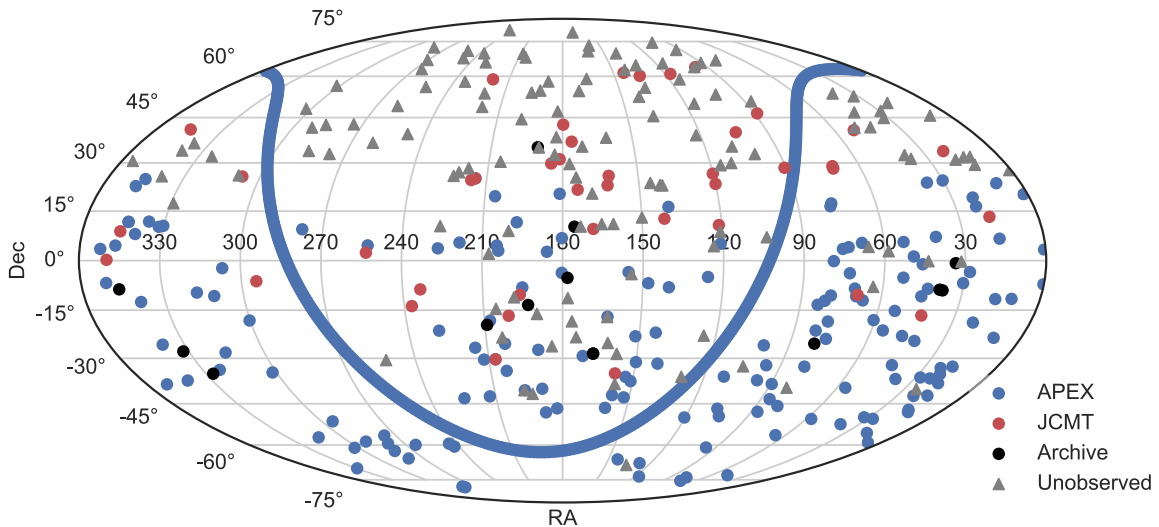


Figure 1. Overview of the AGN galaxies drawn from the 70-month Swift-BAT all-sky catalog relevant for our molecular gas observations (shown in equatorial coordinates and a Mollweide projection). Sources with CO(2–1) observations available either through our APEX or JCMT campaigns, or from the literature, are shown with blue, red, and black circles, respectively. Unobserved sources, mainly in the northern hemisphere, are shown as gray triangles. The Galactic plane is indicated by the light line.

Further studies based on SED modeling, constructed from WISE, Herschel PACS, and SPIRE data, have shown that most of the FIR emission ($>50\%$) at $70\ \mu\text{m}$ originates from star formation for most of the sources (e.g., 76%, Shimizu et al. 2017). The link with star formation also indirectly suggests that AGN activity may be driven by the stochastic accretion of cold gas that should be more prominent among late-type systems (Hopkins & Hernquist 2006). However, a more direct test would be to measure the amount of molecular gas in these systems. This sample is therefore excellent for understanding the link between molecular gas and AGN fueling.

In this study, we focus on a sample of nearby BAT AGN galaxies ($0.01 < z < 0.05$) to test whether the total host-galaxy molecular gas is more prominent among luminous AGN and whether this is a key part of their triggering mechanism. High-quality multiwavelength data and associated products for the BAT AGN and their hosts are now available through the BAT Spectroscopic Survey (BASS; Koss et al. 2017),³¹ including black hole mass measurements, X-ray modeling (Ricci et al. 2017) to measure the intrinsic AGN bolometric luminosity and line-of-sight obscuration, and extensive continuum modeling of the FIR emission from Herschel (Meléndez et al. 2014; Mushotzky et al. 2014; Shimizu et al. 2016, 2017). In this paper, we present the CO(2–1) observations of 213 BAT AGN galaxies to study the relationship between black hole growth and host-galaxy molecular gas. Throughout this work, we adopt $\Omega_{\text{M}} = 0.3$, $\Omega_{\Lambda} = 0.7$, and $H_0 = 70\ \text{km s}^{-1}\text{Mpc}^{-1}$.

2. Survey Description, Samples, and Data Reduction

2.1. AGN Sample

Our AGN parent sample consists of 836 ultrahard-X-ray-selected (14–195 keV) AGN included in the 70-month Swift-BAT all-sky catalog (Baumgartner et al. 2013). Of these, we focused on 348 un-beamed AGN with low Galactic

extinction [$E(B - V) < 0.5$] and in a redshift range of $0.01 < z < 0.05$. Sources outside of the Galactic plane ($b > 10^\circ$) were given higher priority, but in seven cases, sources with low Galactic extinction within the Galactic plane were observed. The lower redshift bound was chosen so that a single pointing would recover most of the CO flux from the host galaxy (see relevant angular scales below), while the higher redshift bound was chosen to guarantee a high detection rate within a reasonable integration time. The results for the complementary sample of $z < 0.01$ BAT AGN galaxies are presented in Rosario et al. (2018). In total, 200 AGN galaxies were newly observed—165 with the Atacama Pathfinder Experiment (APEX) and 35 with the James Clerk Maxwell Telescope (JCMT)—while 13 were obtained from the literature. Figure 1 gives an overview of the sky distribution of the 213/348 (61%) observed and the 135/348 (39%) unobserved AGN galaxies between $0.01 < z < 0.05$. A further study of BAT AGN galaxies in the northern hemisphere ($\delta > 0^\circ$), based on the IRAM 30 m telescope, will appear in a future publication (T. Shimizu et al. 2021, in preparation). An ALMA campaign on 32 BAT AGN galaxies in CO (2–1) has also recently been completed (T. Izumi et al. 2021, in preparation).

2.1.1. APEX Observations

APEX 12 m antenna observations were taken for 165 AGN galaxies, comprised of multiple 400 s long integration frames, with a $100''$ throw between the ON and OFF beam. The program totalled 254 hr with 2288 400 s long scans, taken over 67 days between 2016 March and 2017 September. Observing conditions had precipitable water vapor (PWV) ranging from 0.4 to 4.5 mm with a median of 1.5 mm. The observing programs involved were mainly an ESO Large program (PI M. Koss, ~ 150 hr), a follow-up ESO program (PI B. Trakthenbrot, ~ 50 hr), and Chilean time (PI E. Treister, ~ 75 hr). In addition to our own programs, we also reduced data from archival programs for six BAT AGN galaxies, of which only the

³¹ <http://www.bass-survey.com>

spectrum of IC 5063 was already published (Morganti et al. 2013).

We observed the CO(2–1) transition ($\nu_{\text{rest}} = 230.538$ GHz) using the Swedish Heterodyne Facility Instrument (SHFI; Vassilev et al. 2008) with the eXtended Fast Fourier Transform Spectrometer (XFFTS) backend (213–275 GHz), tuned to the source-specific redshifted CO line frequencies. At the observed frequencies (~ 220 – 229 GHz), the APEX effective primary beam size is $26''.3$ – $27''.5$ half power beamwidth (HPBW), corresponding to scales between 6 and 27 kpc at the distances of our sources. Observations were terminated either after (1) a 5σ line detection was reached, (2) ~ 3 hr of observations (including overheads; i.e., 40 minutes on-source), or (3) a sensitivity of 1 mK rms in the antenna temperature scale (T_A^*) (corrected for atmospheric attenuation, the forward efficiency, and signal band gain) in a 50 km s^{-1} channel was reached (whichever criterion came first).

The data were reduced using CLASS, a package of the GILDAS³² programming language. Each 400 s long scan was examined by hand, and they were rejected when they had baseline ripples that clearly did not originate from astronomical sources, or when they showed strong artifacts at the edge of the spectral range ($\pm 1000 \text{ km s}^{-1}$). On average, about 10% of the individual scans of each target were discarded, and in extreme cases, up to 50% of the frames. Flux densities were derived assuming a constant conversion factor of $39 \text{ Jy beam}^{-1} \text{ K}^{-1}$ for the APEX telescope.³³

2.1.2. JCMT Observations

JCMT observations of the CO(2–1) molecular line were taken for 35 AGN galaxies, between 2011 February and 2013 April. Archival data for one additional galaxy were also reduced (NGC 6240). We used the A3 (211–279 GHz) receiver with the ACSIS spectrometer with a beam size of $20''.4$ HPBW. Each galaxy was initially observed for 30 minutes. For weak detections, additional observations were obtained, but totalling no more than 2 hr per target. The individual scans for each target were first-order baseline-subtracted and then coadded. The narrow spectral coverage of the ACSIS ($\sim 1300 \text{ km s}^{-1}$) does not cover enough line-free regions to enable an estimation of the spectral noise, and therefore we added a 10% error to the uncertainty on the line fluxes to account for any spectral baselining uncertainties (e.g., Rosario et al. 2018). The RxA3 observations took place in weather band 5 ($\tau_{225 \text{ GHz}} = 0.20$ – 0.32). Flux densities were derived assuming a constant conversion factor of $28 \text{ Jy beam}^{-1} \text{ K}^{-1}$ (i.e., an aperture efficiency of 0.55).

2.1.3. Literature Measurements

We incorporate 13 literature CO line measurements of AGN galaxies from our parent BAT AGN sample, which we did not reobserve (see Table 2). This includes two CO(2–1) observations from the 15 m Swedish ESO Sub-millimeter Telescope (SEST; HPBW = $23''$ at 230 GHz) published in Strong et al. (2004), two from the JCMT published in Papadopoulos et al. (2012), and five from the Caltech Submillimeter Observatory (CSO; HPBW = $32''$) published in Monje et al. (2011). Finally, we also include four AGN galaxies from IRAM that were previously published (Bertram et al. 2007), but we use the

CO(1–0) line (HPBW = $22''$) to avoid the smaller beamwidth associated with the CO(2–1) line.

3. Measurements

The principal analysis steps following the data reduction involve integrated measurements of the CO(2–1) line for each AGN galaxy in our sample, as well as line measurements using simple (Gaussian) profile fitting, to derive CO line properties. These spectral measurements are performed consistently for all 200 AGN galaxy observed with either APEX or JCMT. For the 13 literature measurements, we have only applied beam corrections to the integrated measurements (see Section 3.4). The new CO measurements are complemented with the rich collection of ancillary data available for our BAT AGN through BASS (Section 3.3). We finally describe the sample of inactive galaxies we use for comparison (Section 3.5).

3.1. Integrated Measurements

We measure the velocity-integrated line flux S_{CO} (in units of Jy km s^{-1}) from the reduced spectra by summing the signal within a spectral range defined by hand, following the technique in xCOLD GASS (Saintonge et al. 2017). If the CO(2–1) line is undetected or very weak, the window is set to a width of 300 km s^{-1} to estimate uniform upper limits. The CO line luminosities are then calculated following the relation

$$L'_{\text{CO}(2-1)} = 3.25 \times 10^7 S_{\text{CO}(1-0)} \nu_{\text{obs}}^{-2} D_L^2 (1+z)^{-3}, \quad (1)$$

as given in Solomon et al. (1997), where the line luminosity L'_{CO} (in K km s^{-1}) is derived from the velocity-integrated line flux, $S_{\text{CO}} \Delta v$ (in Jy km s^{-1}) and the luminosity distance, D_L (in Mpc). The error on the line flux is defined as the rms noise achieved around the CO(2–1) line, in spectral channels with width $\Delta w_{\text{ch}}^{-1} = 50 \text{ km s}^{-1}$, and W_{CO} is the width of the CO(2–1) line in km s^{-1} . The detection threshold is set to $S/N = 3$. We provide three examples of CO line detections and nondetections in Figures 2 and 3, respectively. For 15 sources characterized by particularly narrow CO emission, we produced a higher resolution spectrum to optimize the profile fit using either 5, 10, or 20 km/s binning. The complete sample of CO line measurements is found in the online figure set associated with Figure 2.

3.2. Line Fitting

We have additionally measured the line widths ($W_{50 \text{ CO}(2-1)}$) and systemic velocities using Gaussian profile fitting for the detected sources, following the same approach as used in the xCOLD GASS studies (Tiley et al. 2016). Each reduced spectrum is first fit with a single Gaussian through Monte Carlo minimization, using the SHERPAPython package in CIAO4.11. As discussed in Tiley et al. (2016), a symmetric Gaussian double-peak function may be more appropriate for higher S/N spectra, as it minimizes potential biases as a function of S/N, inclination (apparent width), and rotation velocity (intrinsic width). We therefore also fit each spectrum with a Gaussian double-peak function (a parabolic function surrounded by two equidistant and identical half-Gaussians forming the low- and high-velocity edges of the profile), which reduces to a single Gaussian in the limit where the half-width of the central parabola is zero. We report the results obtained from the fitting method that provides the

³² <http://www.iram.fr/IRAMFR/GILDAS>

³³ <http://www.apex-telescope.org/telescope/efficiency/>

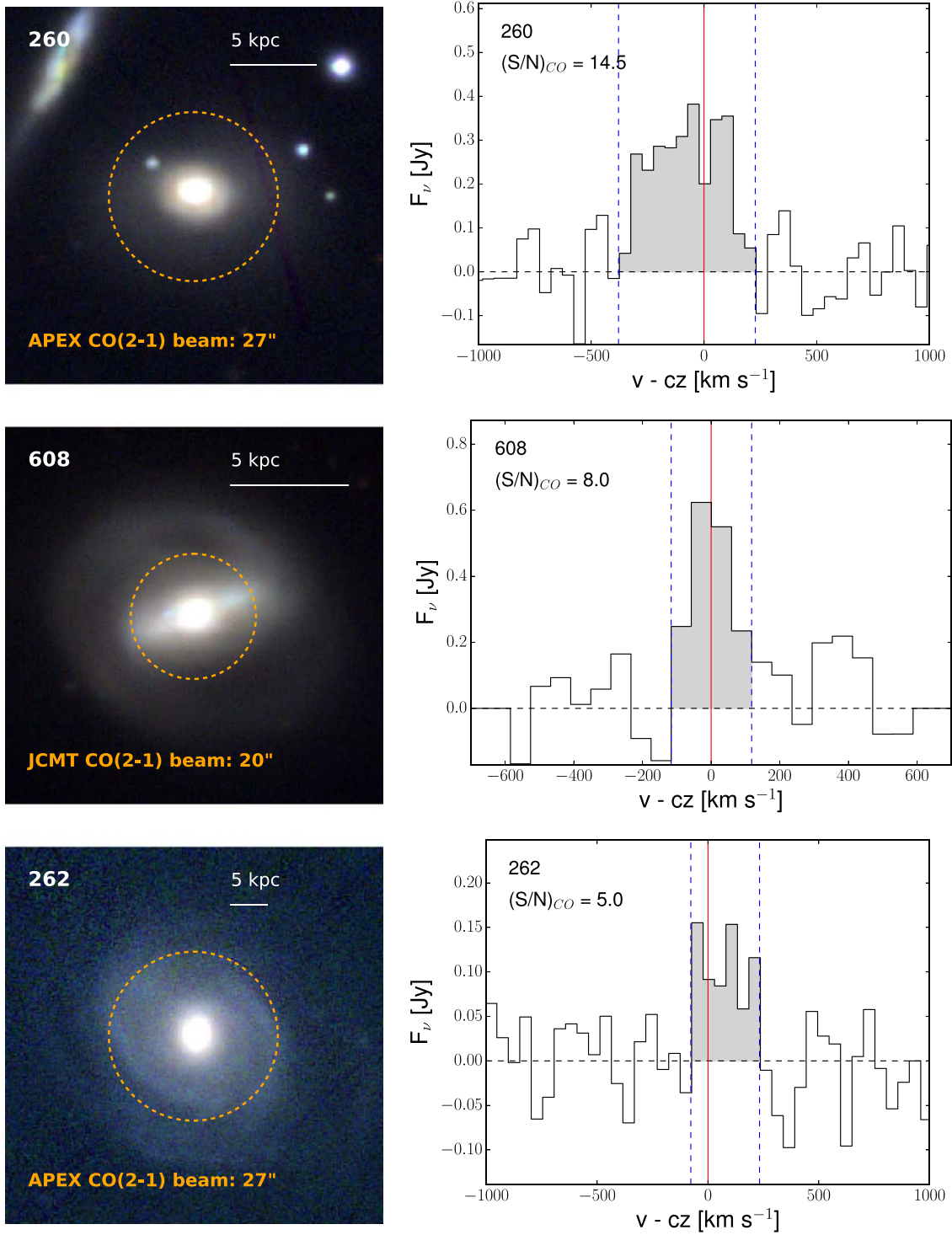


Figure 2. Examples of CO(2–1) detections for three of our BAT AGN galaxies. Left: Pan-STARRS $1' \times 1'$ *gri* color cutouts of the three AGN galaxies, with the beam size of the CO observations marked in orange. Right: CO(2–1) spectra of the same BAT AGN galaxy. The spectra are centered at the position of the CO(2–1) line. Solid red lines mark the central velocity of the optical redshift of each AGN or H I of the host galaxy which was set at the central velocity (cz), while the dashed blue lines indicate the velocity range within which we have integrated the CO(2–1) line fluxes. The three AGN galaxies shown here illustrate CO signal-to-noise ratios typical of the top quartile, median, and bottom quartile of the sample of 151 detections (from top to bottom; $S/N = 14.5$, 8.0 , and 5.0 , respectively). The figure set including all detections and nondetections (200 images and all associated CO(2–1) spectra) is available in the online version of this paper.

(The complete figure set (200 images) is available.)

lowest $|\chi_\nu^2|$ (where χ_ν^2 is the χ^2 of the fit divided by the degrees of freedom). We show three examples of line fits in Figure 4. We find good agreement between profile fitting and integrated measures (see Appendix D).

3.3. Ancillary AGN and Host Galaxy Properties from BASS

We complement the new CO measurements with various galaxy and AGN physical properties, drawn from BASS (Koss et al. 2017)—a large effort to collect optical and X-ray spectra

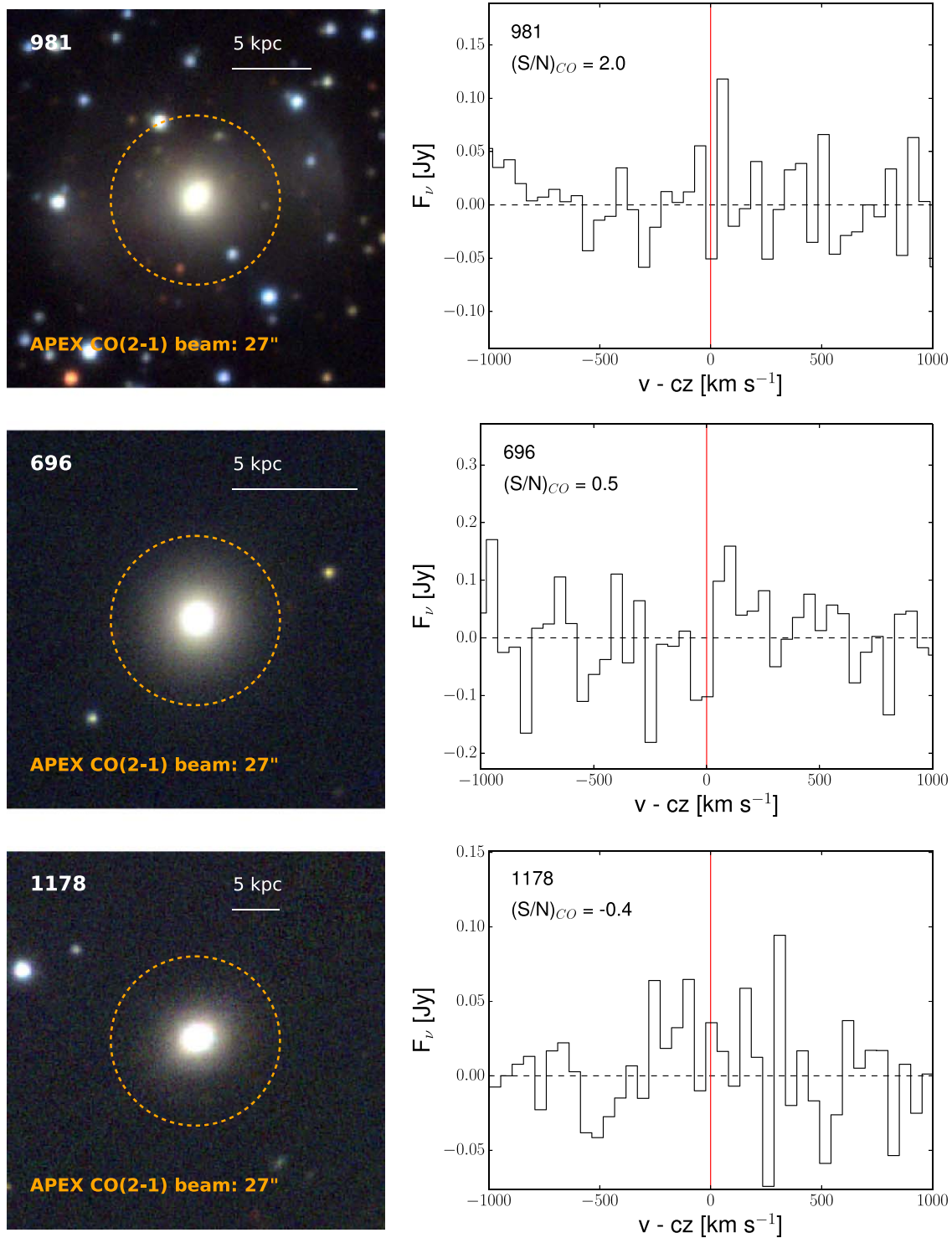


Figure 3. Similar to Figure 2, but for nondetections of the CO(2–1) line, for 3 of our BAT AGN galaxies. Here, the examples also illustrate the typical S/N in the top quartile, median, and bottom quartile among the 63 AGN galaxies with CO nondetections ($S/N = 2, 0.5,$ and -0.4 , respectively).

(Ricci et al. 2017) and various other measurements for Swift-BAT AGN, in order to assess black hole masses, accretion rates, and bolometric luminosity estimates for an unbiased local AGN sample. Optical spectra can be accessed through the BASS website.³⁴ We incorporate products from both Data Releases 1 (DR1) and 2 (DR2); DR1 is currently publicly available, while

DR2 will be published in the near future (M. Koss et al. 2021, in preparation). For all the BAT AGN galaxies in our sample, we use the following key parameters (see Appendix B for a further discussion of the uncertainties in parameter estimation), listed in Table 1 or in associated BASS publications:

1. BAT ID: Catalog ID in the BAT survey.³⁵

³⁴ <http://www.bass-survey.com>

³⁵ <https://swift.gsfc.nasa.gov/results/bs70mon/>

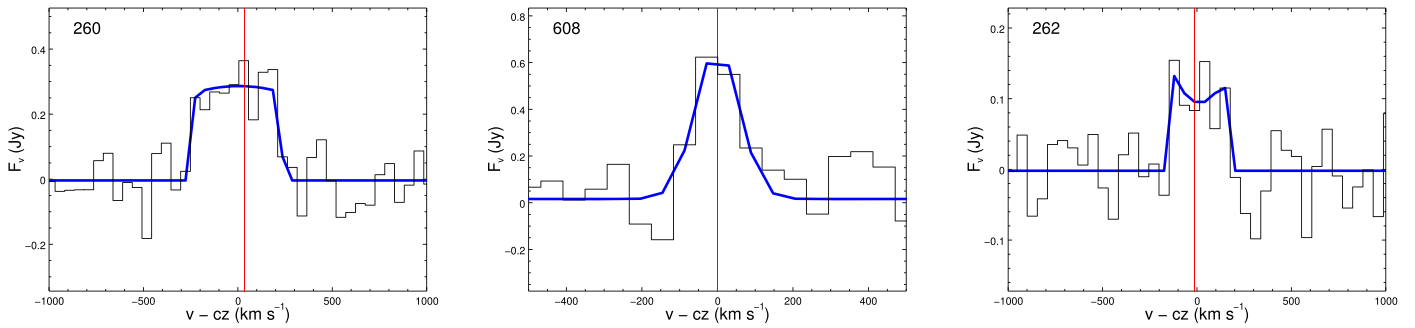


Figure 4. CO(2–1) line profile fits to detected BAT AGN galaxies for the same sources shown in Figure 2, representing the top quartile, median, and bottom quartile of S/N among our detected sample. BAT AGN galaxy IDs 260 (left) and 262 (right) are best fit with a Gaussian double-peak function (a parabolic function surrounded by two equidistant and identical half-Gaussians forming the low- and high-velocity edges of the profile), while BAT AGN galaxy ID 608 (center) is best fit with a single Gaussian. The vertical red lines indicate the central velocity of the CO(2–1) line.

2. α_{J2000} and δ_{J2000} : Right ascension and decl. of the optical/IR counterpart of the BAT AGN, in decimal degrees, based on WISE positions.
3. AGN type and redshift: Measurements from BASS/DR1 (Koss et al. 2017) and DR2 (K. Oh et al. 2021, in preparation), when available. The redshift is based on optical emission-line fitting (mainly of [O III] $\lambda 5007$). While the emission-line redshifts may have an offset from the systemic host velocities (Rojas et al. 2020), they provide a rough estimate of the likely CO centroid.
4. r_{k20fe} : The isophotal radius at a surface brightness of 20 mag arcsec⁻² in the *K* band, taken from the 2MASS extended source catalog (Jarrett et al. 2000).
5. Inclination angle: Galaxy inclination angle based on *r*-band optical imaging from the SDSS, Kitt Peak (Koss et al. 2011a), or from the 2MASS extended source catalog (Jarrett et al. 2000). In order to determine the inclination from the observed ratio of the semiminor to semimajor axes of the galaxy, we use the prescription of Davis et al. (2011) for both early- and late-type galaxies.
6. Morphology: Morphological classification from Galaxy Zoo (Lintott et al. 2008), when available, followed by the Third Reference Catalog of Bright Galaxies (RC3, de Vaucouleurs et al. 1995), and finally visual inspection following the approach of Koss et al. (2011a), which is based on optical imaging. Values can be “elliptical,” “spiral,” or “uncertain.” See Appendix A for a further discussion of the uncertainty in morphology measures.
7. Stellar mass: Stellar masses of the BAT AGN host galaxies. We combined near-IR data from 2MASS, which is more sensitive to stellar emission, with mid-IR data from the AllWISE catalog (Wright et al. 2010), which is more sensitive to AGN emission (i.e., reprocessed by the circumnuclear dusty gas). See Powell et al. (2018) for a further description of these measurements.
8. Star formation rate: The majority (80%, 171/213) of SFR estimates were derived from the Herschel-based study of BAT AGN galaxies by Shimizu et al. (2017), which measured the total IR (8–1000 μm) luminosities by decomposing the IR SEDs into AGN- and galaxy-related components using WISE (3.4, 4.6, 12, and 22 μm), Herschel PACS (70 and 160 μm) and SPIRE (250, 350, and 500 μm) imaging. A subset of 19% (40/213) AGN galaxies were not part of this Herschel imaging

publication. For these we adopt the results of Ichikawa et al. (2019), who performed a similar IR SED decomposition but included any available WISE, Akari, IRAS, and Herschel measurements. While both studies have similar values, we preferentially use the Herschel-based measurements of Shimizu et al. (2017) to avoid the much larger PSF of the IRAS data compared to the CO. Ultimately, 15/213 (7%) of the SED estimates are only upper limits because no FIR detection ($>60 \mu\text{m}$) was found. Additionally, 3/213 (1%) sources lie within 10° of the Galactic plane and were not part of either study. See Appendix B for a further discussion about the uncertainties and offsets in SFR measurements.

9. Offset from the main sequence of star formation: A correlation between stellar mass and SFR has been found for galaxies in the local and distant universe (see review in, e.g., Tacconi et al. 2020). The offset, $\Delta(\text{MS})$, is defined as the difference on a logarithmic scale between the observed SFR of a galaxy and its expected SFR in relation to the main sequence (MS) from Renzini & Peng (2015). A value of $\Delta(\text{MS}) = 1$ would indicate that a galaxy is elevated above the expected value of SFR on the MS by a factor of 10, while $\Delta(\text{MS}) = -1$ indicates a factor of 10 lower than expected.

3.4. Beam Corrections

Beam corrections are needed because the lowest redshift galaxies ($z \sim 0.01$ – 0.02) with the largest angular sizes may have more flux extending outside of the beam that goes unmeasured compared to more distant sources ($z \sim 0.04$ – 0.05) with smaller angular sizes, where most or all of the CO(2–1) flux is likely recovered.

For each galaxy we estimate an aperture correction separately using a model of the gas distribution and either Herschel/PACS imaging (Lamperti et al. 2019) or the galaxy diameter from the *K*-band effective radius (see Saintonge et al. 2011b, 2017, for more details on this technique). For the majority of the sample (81%, 179/213), we use Herschel/PACS imaging. We assume that the CO luminosity is traced by the PACS 160 μm Herschel emission (FWHM = $12''$) from Meléndez et al. (2014). We use the PACS 160 μm images because the longer wavelength is less likely to be contaminated by AGN emission, which can still contribute to a significant

Table 1
Multiwavelength Properties of the BAT AGN Galaxy Sample

ID	Galaxy	α_{J2000} (deg)	δ_{J2000} (deg)	AGN Type	z_{spec}	rk20fe ($''$)	Incl (deg)	Morph	$\log M_*$ ($\log M_\odot$)	SFR ($M_\odot \text{ yr}^{-1}$)	$\Delta(\text{MS})$
3	NGC7811	0.6101	3.35191	Sy1.5	0.033	14.8	41	spiral	10.64	4.68	0.45
17	ESO112-6	7.68262	-59.00721	Sy2	0.0325	15.5	61	spiral	10.56	7.17	0.66
28	NGC235A	10.72004	-23.54104	Sy1.9	0.0158	17.5	38	spiral	10.9	8.05	0.61
44	ESO195-IG021	15.14568	-47.86772	Sy2	0.037	10.3	66	uncertain	10.95	9.48	0.68
50	ESO243-G026	16.40833	-47.07168	Sy2	0.0168	34.8	78	spiral	10.39	2.21	0.21
58	NGC424	17.86516	-38.08345	Sy1.9	0.0163	35.1	83	spiral	10.49	4.72	0.5
62	IC1657	18.52921	-32.65088	Sy2	0.0262	46.6	80	spiral	10.62	3.1	0.27
63	NGC454E	18.60391	-55.39704	Sy2	0.0164	35.2	77	uncertain	10.45	1.57	0.04
72	NGC526A	20.97654	-35.06544	Sy1.9	0.0169	13.9	57	elliptical	10.48	2.23	0.18
77	Mrk359	21.88548	19.17883	Sy1.5	0.0136	16.6	52	spiral	10.5	3.23	0.33
79	CGCG459-058	22.10183	16.45932	Sy2	0.0179	13.2	77	spiral	10.83	11.6	0.79
81	ESO244-IG030	22.46323	-42.32645	Sy2	0.0294	21.4	78	uncertain	10.66	6.25	0.57
83	ESO353-G009	22.96001	-33.11929	Sy2	0.0173	24.3	57	uncertain	10.68	6.13	0.55
95	ESO354-G004	27.92441	-36.18782	Sy1	0.0202	16.5	40	spiral	10.94	3.45	0.24
96	MCG-01-05-047	28.20432	-3.44684	Sy2	0.0249	66.7	89	spiral	10.88	11.65	0.78
101	UGC01479	30.07939	24.47383	Sy2	0.0129	39.1	80	spiral	10.6	3.22	0.3
102	NGC788	30.27691	-6.81588	Sy2	0.0127	37.6	42	elliptical	10.89	1.74	-0.04
114	ESO197-G027	32.71889	-49.69852	Sy2	0.0267	18.5	82	uncertain	11.04	15.65	0.88
116	Mrk 590	33.63984	-0.76672	Sy1.5	0.0289	27.3	41	uncertain	11.2	6.08	0.45
128	MCG+4-6-43	36.72751	23.79966	Sy1	0.0333	13.2	44	spiral	10.8	<1.35	<-0.12

Note. A detailed description of this table’s contents is given in Section 3.3.

(This table is available in its entirety in machine-readable form.)

fraction of the 70 μm emission (e.g., Shimizu et al. 2017; Ichikawa et al. 2019).

We first measure the total infrared 160 μm emission of the galaxy within a radius large enough to include the entire galaxy. Then we take the ratio between the flux from the map multiplied by the CO(2–1) Gaussian beam sensitivity function and the total IR flux, and we use this value to extrapolate the total CO(2–1) flux.

The images that we used to trace the distribution of the FIR emission are not maps of the “true” distribution, but instead are maps of the “true” distribution convolved with the PSF of PACS (12 $''$). Therefore an additional correction is needed.

To correct for the effect of the PACS PSF smearing, we use a simulated galaxy gas profile, following the procedure described in Saintonge et al. (2011b). For each galaxy, we create a model galaxy simulating a molecular gas disk following an exponential profile, with a scale length equivalent to its half-light radius. Then the profile is tilted according to the inclination of the galaxy, and we measure the amount of flux that would be observed from this model galaxy, using an aperture corresponding to the size of the beam. We multiply the IR image by a 2D Gaussian centered on the galaxy center and with FWHM equal to the beam size to mimic the effect of the beam sensitivity of the telescope that took the CO observations. By taking the ratio of these two measurements, we estimate how much the flux changes due to the effect of the FIR PSF smearing. We perform this 160 μm based correction on 69% (148/213) of images. For an additional 7% (15/213), we use the 70 μm surface brightness because the 160 μm was a nondetection.

In cases where the PACS imaging resulted in a nondetection, or where no PACS imaging exist (51/213, or 24%), we directly use the simulated galaxy gas profile discussed above as described in the COLD GASS and xCOLD GASS papers (Saintonge et al. 2011b, 2017) and solely use the K -band

galaxy diameter ($D = 2 \times r_{\text{rk20fe}}$) and inclination to estimate the correction factor. Further discussion of the beam corrections is presented in Appendix C.

3.5. Inactive Galaxy Comparison Sample

As the properties of (molecular) gas in galaxies are known to be related to stellar mass and morphology (e.g., Saintonge et al. 2011b; Young et al. 2011), it is critical that our analysis of the BAT AGN galaxies is done in comparison to a large, unbiased control sample of inactive galaxies spanning a similar range in stellar mass.

The IRAM 30 m xCOLD GASS sample (Saintonge et al. 2017) comprises 532 galaxies from two large IRAM programs, with measurements and analyses of molecular gas across a large range of stellar masses [i.e., $9 < \log(M_*/M_\odot) < 11.5$], and over the same redshift range as our sample of BAT AGN galaxies (i.e., $0.01 < z < 0.05$).

The xCOLD GASS sample is primarily composed of IRAM measurements, meaning that CO(1–0), with a HPBW of $\approx 22''$, is a good match to our APEX (HPBW = 27 $''$) and JCMT (HPBW = 20 $''$) CO(2–1) data, even though a different line is used to probe the molecular gas. The xCOLD GASS sample also contains 28 galaxies with APEX(2–1) measurements, and the authors found that the APEX CO(2–1) to IRAM CO(1–0) luminosity ratio for velocity-integrated measurements is $r_{21} = 0.79 \pm 0.03$, based on robust measurements of both lines, with no systematic variations across the sample properties (e.g., SFR, sSFR, or f_{H_2}). The range typically varies between ~ 0.6 and 1.0 in nearby galaxies (Leroy et al. 2009). We adopt this r_{21} conversion factor to convert our AGN galaxy measurements from CO(2–1) into CO(1–0) before converting into molecular gas. Further analysis of the line ratio will be discussed in T. Shimizu et al. (2021, in preparation), who

reobserved 56 BAT AGN galaxies from our APEX and JCMT sample using IRAM in both CO(1–0) and CO(2–1).

For the purposes of our study, we excluded 164 galaxies with low stellar masses [$\log(M_*/M_\odot) < 10$], which are only rarely present in our BAT AGN galaxy sample. We further ensured that the xCOLD GASS comparison sample does not include any AGN. First, no BAT AGN galaxies were present in xCOLD GASS, likely due to their low space density. Second, we used the SDSS nebular emission-line measurements from the OSSY database (Oh et al. 2011) to test for AGN activity based on strong line diagnostics for the entire xCOLD GASS sample. We identified 14 optically selected AGN based on the [O III]/H β versus [N II]/H α diagnostics of Kewley et al. (2006). We then also checked against the SDSS-based catalog of broad H α line emitters compiled by Oh et al. (2015), but no galaxies were found to be part of this catalog. We finally checked the Veron-Cetty Catalog of Quasars and AGN (Veron-Cetty & Veron 2010) and found that three xCOLD GASS sources were reported as hosting AGN. We also removed four radio-loud AGN galaxies (Best & Heckman 2012). In the process of reviewing the xCOLD GASS sample, we also realized that for three galaxies, the SDSS spectroscopic pipeline inaccurately targeted a spiral arm or other feature and that the nucleus of the galaxy is more than 5'' away. We have excluded these galaxies also because their photometry and measurements are unreliable (ID = 20790, 36169, and 31592). The final xCOLD GASS inactive galaxy comparison sample thus holds 344 inactive galaxies.

Throughout this analysis and for both samples, we adopt a Milky Way-like conversion factor from CO luminosity to H $_2$ mass of $\alpha_{\text{CO}} = 4.3 M_*(\text{K km s}^{-1} \text{pc}^2)^{-1}$ (see e.g., Bolatto et al. 2013 for a review). Studies of nearby galaxies with kiloparsec-scale resolutions have found that α_{CO} is generally flat with galactocentric radius, with average values of 3.1 ± 0.3 for nearby galaxies. While ULIRG-type galaxies are thought to have lower α_{CO} values (e.g., $\alpha_{\text{CO}} \sim 1 M_\odot/(\text{K km s}^{-1} \text{pc}^2)$; Narayanan et al. 2012), none of these sources are part of either sample. Given that the stellar mass–metallicity relation is rather flat over the average stellar mass that we study ($\log M_*/M_\odot > 10.0$, Yates et al. 2012) and the difficulty of measuring metallicity in AGN hosts using emission lines because of contamination, we prefer this simple approach rather than invoking metallicity-dependent gradients and conversion factors (e.g., Accurso et al. 2017).

The median beam correction for all the BAT AGN galaxies is 1.33, which is higher by 16% than the xCOLD GASS survey (1.15), mainly driven by the lower redshift ($\langle z \rangle = 0.026$ versus $\langle z \rangle = 0.036$), and higher stellar masses of the galaxies in the AGN galaxy sample. This is somewhat by design as the redshift range ($z = 0.026\text{--}0.05$) was selected to ensure that the whole galaxy was in the IRAM beam for the most massive galaxies ($\log M_*/M_\odot > 10.0$) in xCOLD GASS. We verified that the results presented throughout the rest of the present study are not significantly affected by inadequate aperture corrections by confirming that the distributions of key quantities and/or relations between them do not depend on galaxy redshift (or distance).

3.6. CO Catalog Description

We provide the full catalog of CO(2–1) measurements and key derived quantities for all 213 BAT AGN galaxies in our sample. A summary of possible trends between the CO

detection fraction and various AGN galaxy properties is provided in Figure 5.

The catalog includes the following quantities, included in Table 2:

1. **BAT ID**: Unique ID in the Swift -BAT 70-month catalog (see footnote 35).
2. **Telescope and HPBW**: The telescope used for the CO observation—either JCMT or APEX for our own observations, or for the archival data, along with the associated beam size.
3. **FlagCO21**: A detection flag for the CO(2–1) line, with “1” indicating a detection, and “0” indicating a nondetection. When the line is not detected, the tabulated line luminosities and molecular gas masses (see below) are 3σ upper limits.
4. **σ_{CO21}** : rms noise achieved around the CO(1-0) line, in spectral channels with width $\Delta w_{\text{ch}} = 50 \text{ km s}^{-1}$. The quoted rms is at 50 km s^{-1} even for spectra with finer binning.
5. **Beam-correction factor**: Beam aperture correction, derived either through simulations following the approach developed for the COLD GASS sample (Saintonge et al. 2011b), or by assuming the CO luminosity is traced by the $160 \mu\text{m}$ emission observed by Herschel/PACS (FWHM = $12''$), as reported by Meléndez et al. (2014).
6. **$L'_{\text{CO21,corr}}$** : Total CO(2–1) line luminosity, calculated from $L'_{\text{CO21,obs}}$ and the aperture correction. The error includes the measurement uncertainty, a 10% flux calibration error, and the 15% uncertainty on the aperture correction (Saintonge et al. 2011b)—all combined in quadrature. If the source is undetected in CO (FlagCO21 = 0 in Col. 3), then the tabulated value corresponds to a 3σ upper limit.
7. **$\log M_{\text{H}_2}$** : Total molecular gas mass, including the helium contribution, calculated from the integrated CO(2–1) line luminosity assuming a conversion of 0.79 from CO(2–1) to CO(1–0), and assuming a Milky Way-like conversion factor of $\alpha_{\text{CO}} = 4.3 M_*(\text{K km s}^{-1} \text{pc}^2)^{-1}$ (Bolatto et al. 2013). If the source is undetected in CO (FlagCO21 = 0 in Col. 3), then the tabulated value corresponds to a 3σ upper limit.
8. **$t_{\text{dep}}(\text{H}_2)$** : The gas-depletion timescale ($t_{\text{dep}}(\text{H}_2) \equiv M_{\text{H}_2}/\text{SFR}$). A small number (8%, 16/207) of AGN galaxies have no measurements (denoted as “...”) because they lack robust SFR measurements. Most of these (14/16) were not observed within the Herschel program, and thus have less sensitive SFR upper limits, or they lie close to the Galactic plane where no measurements were performed (12%, 2/16). Most are also undetected in molecular gas (75%, 12/16). As they have upper limits on SFR and molecular gas, a gas-depletion timescale, which is the ratio of the two, cannot be estimated.
9. **PROTYPE**: CO line measured with either a single- or double-peak Gaussian profile (as indicated by $w_{50\text{type}}$; Tiley et al. 2016).
10. **$L'_{\text{pro,corr}}$** : Total CO(2–1) line luminosity, calculated from the profile fit $L'_{\text{pro,corr}}$ with an aperture correction.
11. **w_{50}, z_{CO}** : FWHM of the line from the profile fit in km s^{-1} , the associated error, and redshift from the central velocity. The tabulated errors correspond to 1σ .

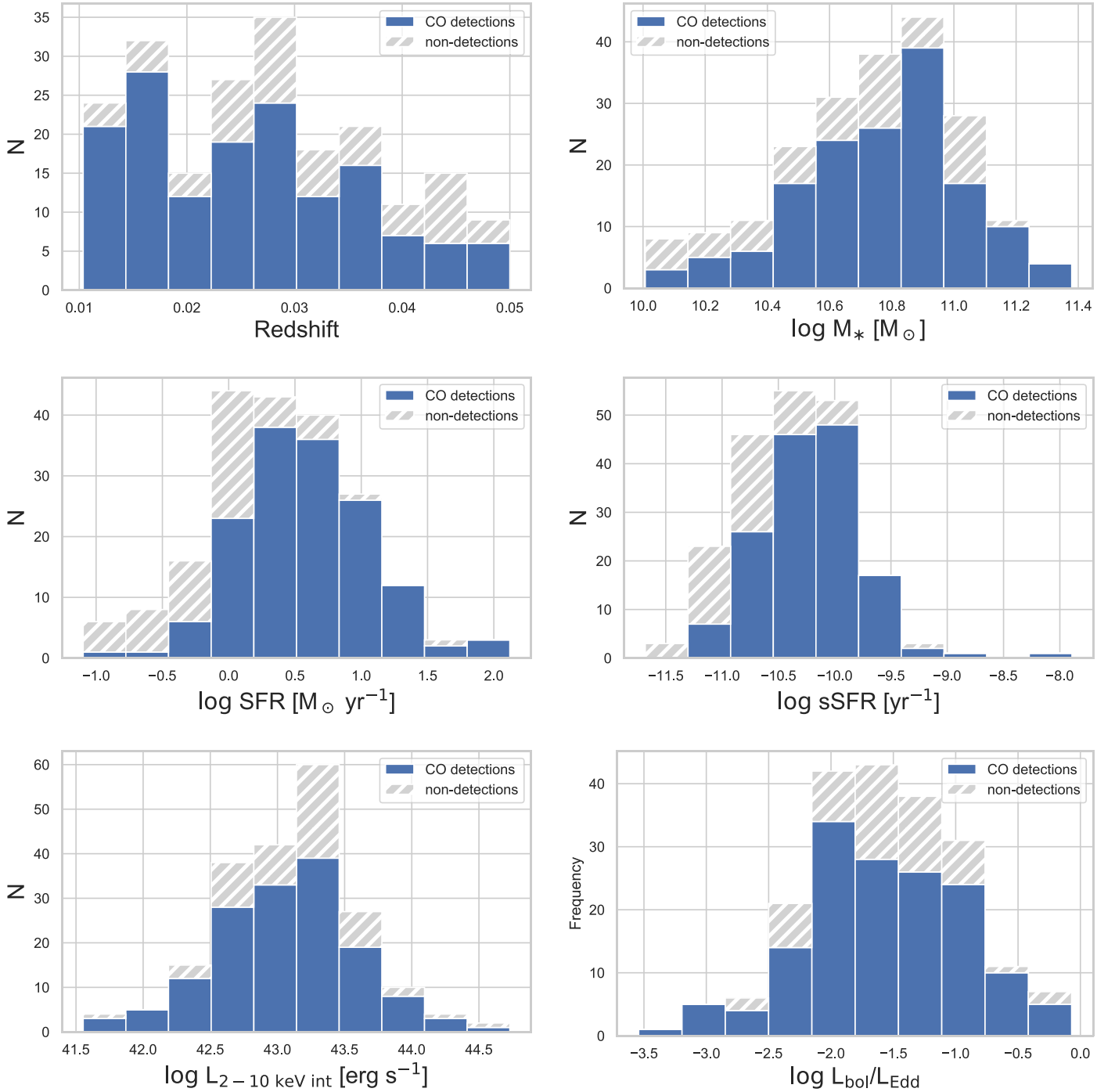


Figure 5. Stacked bar chart distributions of the sample of BAT AGN galaxies, with CO detections (blue) and nondetections (gray) as functions of redshift, host-galaxy stellar mass, SFR, sSFR, intrinsic X-ray luminosity, and Eddington ratio. In nearly all cases, except at low star formation rates ($\text{SFR} < 1 M_\odot \text{ yr}^{-1}$), the majority of the sample is detected.

The full BAT AGN galaxy CO catalog, including all CO spectra, SDSS and PS1 images, and galaxy and ancillary AGN observations from BASS will be available at the BASS website (<http://www.bass-survey.com>).

4. Results

Here we compare the molecular gas properties we measure in our sample of BAT AGN galaxies with those of the inactive galaxies studied within the xCOLD GASS survey. We further search for links between the molecular gas content of our BAT

AGN galaxies and their basic AGN-related properties, such as their intrinsic X-ray luminosity ($L_{2-10 \text{ keV}}^{\text{in}}$) and Eddington ratio ($L/L_{\text{Edd}} \equiv L_{\text{bol}}/L_{\text{Edd}}$). For the purposes of this analysis, we have excluded six BAT AGN that are hosted in galaxies with particularly low stellar mass compared with the overall sample ($\log(M_*/M_\odot) < 10.0$; see Figure 5). A comparison of low stellar mass BAT AGN galaxies with inactive galaxies, at $z < 0.01$, can be found in Rosario et al. (2018). Our final BAT AGN galaxy sample thus totals 207 AGN galaxies with $\log(M_*/M_\odot) > 10.0$.

Table 2
Catalog of CO(2–1) Measurements

ID	Tele.	HPBW ($''$)	Flag	σ (mK)	C_{aper} Factor	S/N_{inte}	$L'_{\text{inte,corr}}$ ($10^8 \text{ K km s}^{-1} \text{ pc}^2$)	$\log M_{\text{H}_2}$ ($\log M_{\odot}$)	$t_{\text{dep}}(\text{H}_2)$ (log yr)	Pro_{type}	$L'_{\text{pro,corr}}$ ($10^8 \text{ K km s}^{-1} \text{ pc}^2$)	S/N_{pro}	W50 (km s^{-1})	z_{CO} (km s^{-1})
3	APEX	27	1	1.8	1.05	5.5	3	9.11	8.44	1	3	3.2	74 ± 21	7659 ± 10
17	APEX	27	1	0.9	1.04	11	7.7	9.52	8.66	2	8.1	10.4	561 ± 158	8614 ± 55
28	APEX	27	1	1.7	1.31	14.4	11.7	9.7	8.79	2	11.4	12.5	461 ± 94	6604 ± 42
44	APEX	27	1	1.3	1.21	7.4	25.2	10.03	9.05	2	23	9.2	469 ± 123	14363 ± 56
50	APEX	27	1	1.1	1.16	7	2.9	9.1	8.75	2	4.8	11.9	559 ± 160	5737 ± 51
58	APEX	27	1	0.8	1.51	6	0.7	8.5	7.83	1	0.6	6.2	499 ± 237	3408 ± 79
62	APEX	27	1	2	1.78	16.3	5.7	9.39	8.9	2	4.7	7.8	304 ± 59	3572 ± 26
63	APEX	27	1	0.8	1.17	7	0.9	8.61	8.41	1	0.5	5.7	158 ± 135	3634 ± 18
72	APEX	27	1	0.7	1.19	4.3	1	8.63	8.28	1	1.7	8	601 ± 252	5748 ± 83
77	APEX	27	1	2.1	1.3	8.4	4	9.24	8.73	1	4	5.8	86 ± 23	5075 ± 7
79	APEX	27	1	1.1	1.02	10.7	14.6	9.79	8.73	2	14.9	10.2	522 ± 121	11416 ± 52
81	APEX	27	1	1.3	1.35	13.2	9.6	9.61	8.82	2	10.2	9.9	381 ± 120	7707 ± 42
83	APEX	27	1	4.4	1.11	12.8	10.3	9.64	8.86	1	11.1	9.9	268 ± 56	4934 ± 23
95	APEX	27	1	1	1.06	6.8	5.9	9.41	8.87	2	6.2	8.4	409 ± 166	10033 ± 54
96	APEX	27	1	2.9	2.19	8.4	12.8	9.74	8.67	1	10.5	7.9	281 ± 83	5006 ± 32
101	APEX	27	1	2.1	1.21	9.2	4.8	9.32	8.81	1	5.3	10.2	323 ± 62	4903 ± 31
102	APEX	27	1	0.5	2.88	5.9	1	8.66	8.41	1	0.4	2.2	42 ± 35	4170 ± 9
114	APEX	27	1	0.9	1.42	12.4	26.4	10.05	8.86	2	24.5	8.8	533 ± 115	14295 ± 60
116	APEX	27	1	1.3	1.52	11.2	8.4	9.56	8.77	2	10.1	8.4	252 ± 44	7926 ± 19
128	APEX	27	1	1.2	1.04	4.7	3.4	9.16	...	1	3	3	48 ± 54	10069 ± 7

Note. A detailed description of this table's contents is given in Section 3.6.

(This table is available in its entirety in machine-readable form.)

As our sample includes a significant number of CO nondetections, and thus upper limits on a few key derived quantities (CO luminosities and molecular gas mass), our analyses of distributions and correlations rely on a survival analysis. Specifically, we have used the Kaplan–Meier (KM) distribution to perform a survival analysis using the software `lifelines` Python package version 0.25.4 (Davidson-Pilon et al. 2020). In what follows, we test for statistically significant differences using the KM estimator, which is similar to the standard Kolmogorov–Smirnov test, but allows for left-censoring (i.e., upper limits). We adopt a 5% threshold probability when evaluating the significance of a difference from the null hypothesis between samples (i.e., $p < 0.05$) and use this test to compare all sample differences. In order to ensure that the sample tests are not sensitive to the specific upper limit level, we reran significance tests assuming the upper limits were larger or smaller by 30%, and noted any differences when they occurred.

4.1. Molecular Gas Content—Comparison to Inactive Galaxies

As shown in Figure 6, our sample of BAT AGN galaxies strongly skews toward higher stellar masses compared to the xCOLD GASS sample of inactive galaxies [$\log(M_*/M_\odot) = 10.75 \pm 0.02$ versus $\log(M_*/M_\odot) = 10.58 \pm 0.02$, respectively]. Importantly, considering the regime where most BAT AGN galaxies reside ($\log(M_*/M_\odot) > 10.5$), the median molecular gas mass and molecular gas fraction are systematically higher in BAT AGN galaxies than in the inactive galaxies at fixed stellar mass ($p < 0.001$; right panels of Figure 6). Additionally, the BAT AGN galaxies typically lie on the MS of star-forming galaxies compared to inactive galaxies in xCOLDGASS, which lie below it for the majority of the sample ($p < 0.001$, $\log(M_*/M_\odot) > 10.2$).

In Figure 7 we present the molecular gas content of the BAT AGN galaxies and the xCOLD GASS inactive galaxies in the context of other star formation properties. The AGN galaxies clearly occupy a region of elevated star formation (both in terms of SFR and sSFR). In particular, passive galaxies—i.e., those with $\log(\text{sSFR}/\text{yr}^{-1}) < -11$ —are a distinct minority among our BAT AGN galaxies (2%–7%, due to upper limits), whereas they comprise roughly half of the inactive galaxies (49%). Over the limited range of SFRs where the two samples overlap ($0.2 < \log(\text{SFR}/M_\odot \text{ yr}^{-1}) < 0.7$), the amount of molecular gas is not significantly different between the inactive galaxies and AGN galaxies. The gas fractions at a given sSFR are lower for AGN galaxies than for inactive galaxies ($p = 0.004$), however. The gas-depletion timescales [$t_{\text{dep}}(\text{H}_2) \equiv M_{\text{H}_2}/\text{SFR}$] for AGN galaxies are not significantly different.

In Figure 8 we show the molecular gas and gas fraction timescales, and the depletion timescale with offset from the MS as defined by Renzini & Peng (2015). The BAT AGN tend to largely lie on this MS. The xCOLDGASS inactive galaxies have a much larger fraction of galaxies significantly below the MS consistent with their lower average SFR. Over the limited range in which the two samples overlap in offset from the MS ($-0.5 < \Delta(\text{MS}) < 0.5$), the AGN galaxies have lower gas fractions ($p < 0.01$), but not significantly different molecular gas masses or depletion timescales.

4.1.1. Galaxy Molecular Gas Luminosity Function

Another way to study how important molecular gas is to AGN activity is to compare the number of AGN galaxies with a given molecular gas mass for a given volume to the number of inactive galaxies. We do this by comparing the CO luminosity function from xCOLD GASS (see Figure 2, Fletcher et al. 2020), which was constructed to measure the molecular gas of all galaxies of a given stellar mass ($\log(M_*/M_\odot) > 9.0$). The mass function was then created by normalizing to match the stellar mass function of local galaxies, and thus be representative of local galaxies. The BAT AGN galaxy sample is then a subset of this local galaxy sample for all galaxies hosting an AGN above a certain X-ray luminosity across the sky. As the BAT sample is flux limited, we use the V_{max} correction method following Ananna et al. (2020) to estimate the correction factor for each BAT AGN galaxy based on the observability of its intrinsic X-ray flux within the volume studied ($0.01 < z < 0.05$) and the sensitivity of BAT across the sky (Baumgartner et al. 2013). We focus on the 144 more luminous AGN galaxies ($L_{2-10 \text{ keV}}^{\text{in}} > 10^{42.8} \text{ erg s}^{-1}$ or $L_{\text{bol}} > 10^{44} \text{ erg s}^{-1}$) in the sample where the survey sensitivity can detect sources in the majority of the volume surveyed and the V_{max} corrections are less uncertain. We also correct for the unobserved BAT AGN galaxies (39%) and the volume near the Galactic plane that was excluded ($b < 10^\circ$).

The likelihood of a given galaxy hosting a luminous AGN clearly increases with gas mass (Figure 9), but the absolute fraction maxes out at 1%–10% even among the most gas-rich sources. Presumably, key factors such as the gas distribution, stochasticity, and ability to lose angular momentum play essential roles.

4.1.2. Morphological Comparison

We next consider the molecular gas properties of the BAT AGN hosts and the xCOLD GASS inactive galaxies as a function of their morphologies (spiral, elliptical, and “uncertain”), as shown in Figure 10. For reference, we provide example images of elliptical, uncertain, and spiral host morphologies in Appendix A.

Among spiral galaxies, the molecular gas masses and gas fractions are similar for both AGN galaxies and inactive galaxies, except at the highest stellar mass bins ($\log(M_*/M_\odot) > 10.8$), where AGN hosts have significantly more molecular gas ($p = 0.001$). For galaxies of uncertain morphologies, the difference between AGN and inactive galaxies extends across all stellar masses ($p < 0.001$), although the offset is not as large as the ellipticals. On the other hand, the difference in molecular gas content of BAT AGN ellipticals and xCOLD GASS ellipticals is profound across all stellar masses studied ($p < 0.001$). Roughly half (51%, 21/41) of the BAT AGN galaxies with elliptical morphology hosts contain significant molecular gas mass reservoirs [$\log(M_{\text{H}_2}/M_\odot) > 9$], compared to almost no gas-rich ellipticals in the xCOLD GASS inactive sample (4%, 3/81).

Both the median molecular gas mass [$\log(M_{\text{H}_2}/M_\odot) = 8.91_{0.17}^{+0.44}$ versus $\log(M_{\text{H}_2}/M_\odot) < 8.4$] and the gas fraction [$\log f_{\text{H}_2} = -1.71_{0.38}^{+0.24}$ versus $\log f_{\text{H}_2} < -2.71$] are significantly higher for elliptical hosts of AGN than for inactive ellipticals ($p < 0.001$), while the gas-depletion timescales [$\log(t_{\text{dep}}(\text{H}_2)/\text{yr}) = 8.88_{0.12}^{+0.15}$ versus $\log(t_{\text{dep}}(\text{H}_2)/\text{yr}) < 8.5$] appear to be lower for inactive galaxies ($p = 0.001$), although we find this

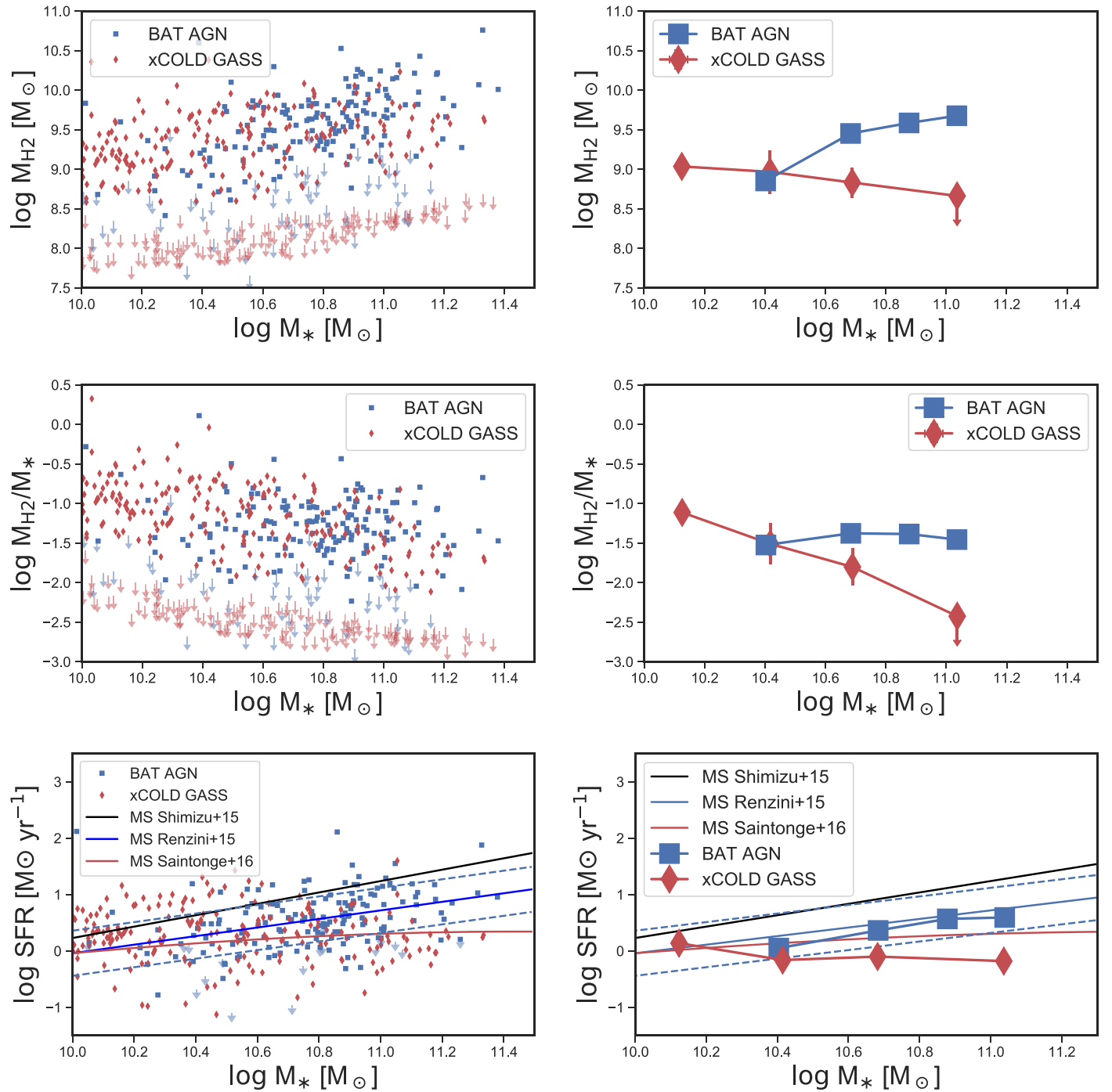


Figure 6. Comparison of molecular gas content, SFR, and stellar mass between BAT AGN hosts and xCOLD GASS inactive galaxies. The top panels show molecular gas masses vs. stellar masses, and the middle panels show molecular gas mass fractions (M_{H_2}/M_*) vs. stellar masses. The bottom panels show the SFR vs. stellar masses. The solid line represents the MS of star-forming galaxies as determined by Renzini & Peng (2015), and the dashed lines indicate the 0.4σ scatter around this line. Due to the significant uncertainty at high stellar masses ($\log(M_*/M_\odot) > 10.5$), we have plotted additional MS lines (Shimizu et al. 2015; Saintonge et al. 2016). The left panels show the individual data points, and the right panels show the data binned in stellar mass. For presentation purposes, in the left panels individual upper limits are shown at the 1σ level, while detections are limited to those with $>3\sigma$. In the right panels, the bin sizes were constructed to have equal numbers of sources in each bin. Error bars on the plotted median values are equivalent to 1σ and calculated based on a bootstrap procedure with 100 realizations. Upper limits on binned data are shown when more than half of the individual data points within that bin are themselves upper limits.

result is not significant when the upper limits are increased by 30%.

Finally, we note that if stricter criteria were used for “uncertain,” the general trends would remain with small differences. The offset in molecular gas properties would be more significant for AGN galaxies in spirals compared to

inactive galaxies. Conversely, the size of the offset would be somewhat smaller for AGN galaxies in ellipticals.

4.2. Molecular Gas Content—Links to AGN Galaxy Properties

Here we examine the molecular gas properties of our BAT AGN galaxy sample as a function of various AGN- and

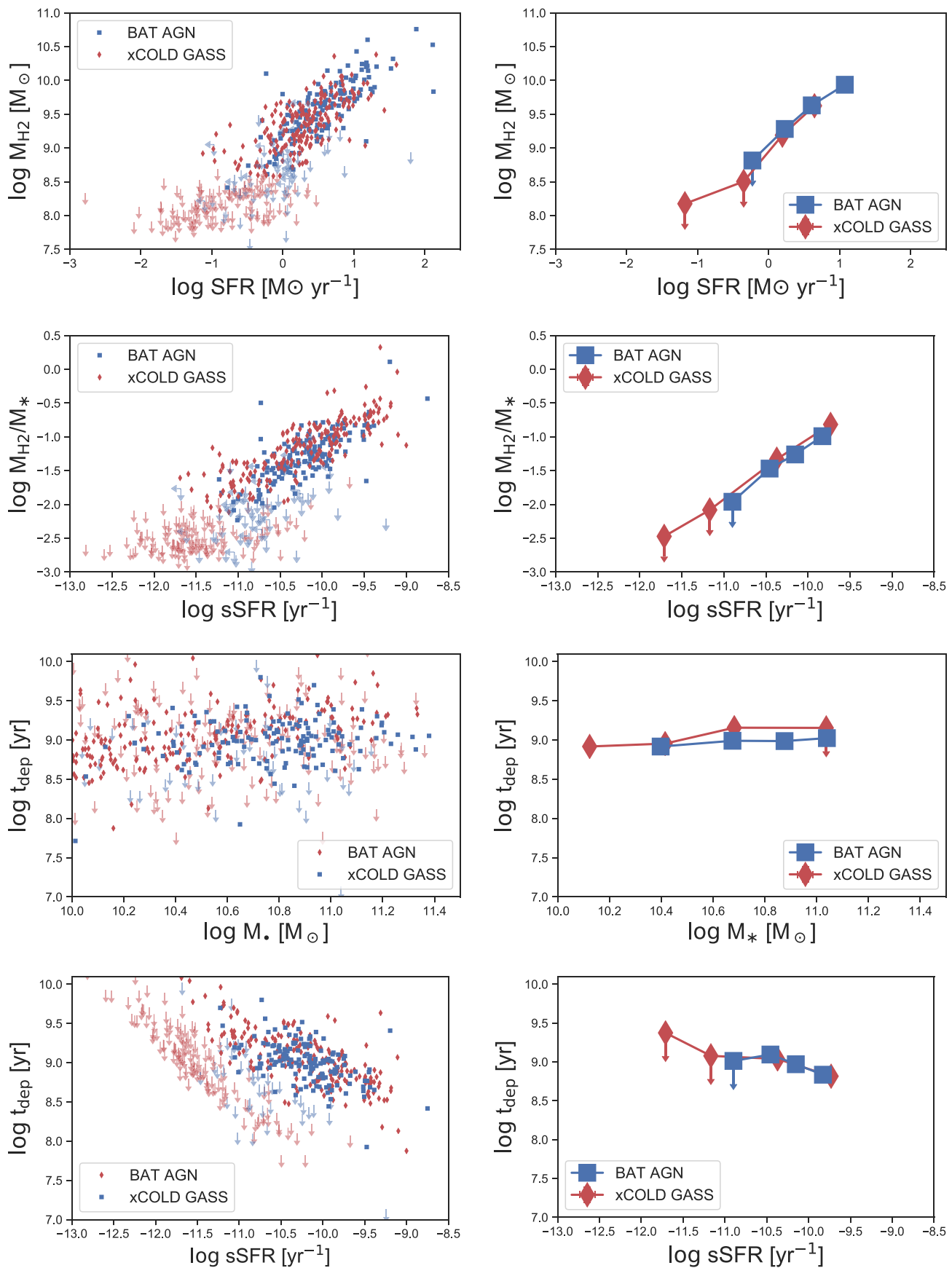


Figure 7. Links between molecular gas content and star formation in BAT AGN galaxies and xCOLD GASS inactive galaxies. The symbols are identical to those of Figure 6, as is the binning procedure used to produce the right column of panels. From top to bottom, we present (1) molecular gas masses vs. SFRs, (2) molecular gas fractions vs. specific SFRs ($\text{sSFR} \equiv \text{SFR}/M_*$), (3) molecular gas-depletion timescales ($t_{\text{dep}}(\text{H}_2) \equiv M_{\text{H}_2}/\text{SFR}$) vs. stellar mass, and (4) depletion timescales vs. sSFRs.

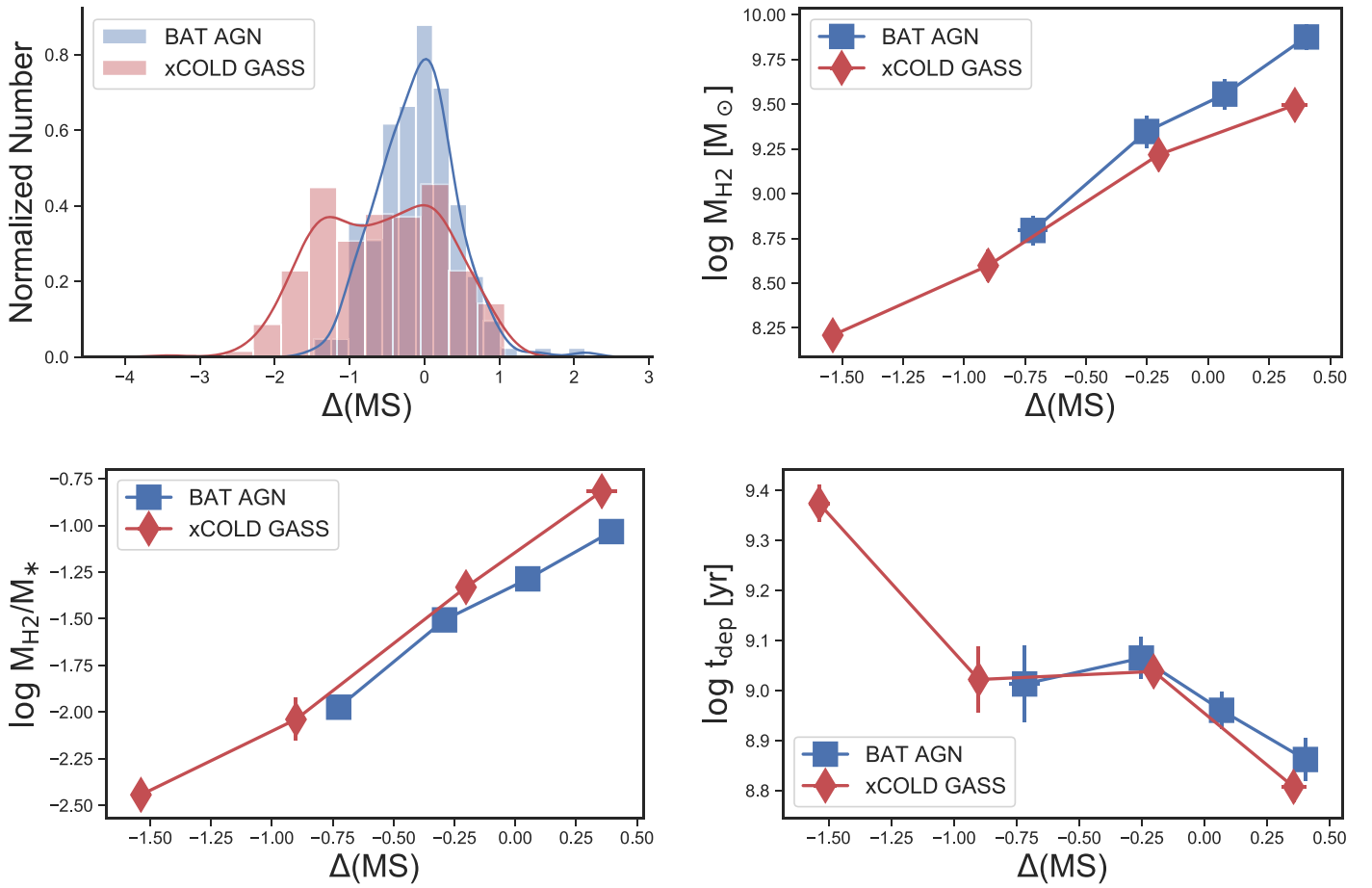


Figure 8. Distribution of offsets from the MS for AGN hosts and inactive galaxies (upper left). The offset, $\Delta(\text{MS})$, is defined as the difference on a logarithmic scale between the observed SFR of a galaxy and its expected SFR in relation to the MS from Renzini & Peng (2015). Links between molecular gas (upper right), gas fraction (bottom left), and depletion timescales (bottom right) in BAT AGN galaxies and xCOLD GASS inactive galaxies as compared to offset from the MS. The symbols and binning procedure are identical to those in the right column of Figure 6.

SMBH-related properties, such as optical AGN classification, intrinsic X-ray luminosity, black hole mass, Eddington ratio, and line-of-sight column density. A summary of the median parameters and confidence limits from the survival analysis for these parameters can be found in Table 3.

4.2.1. Optical AGN Classification

We use the public BASS/DR1 and proprietary DR2 optical spectroscopy available for our AGN to determine their optical, spectroscopic AGN classification. We classify sources that have both broad $\text{H}\alpha$ and $\text{H}\beta$ emission lines as Seyfert 1 s. This includes sources that are often referred to as Type 1.0, 1.5, 1.8 etc. Sources with broad $\text{H}\alpha$ but only narrow $\text{H}\beta$ are classified as Seyfert 1.9 s, and finally, Seyfert 2 s have only narrow Balmer lines. Our BAT AGN sample breaks down as 40% (83/207) Seyfert 1 s, 16% (34/207) Seyfert 1.9 s, and 43% (90/207) Seyfert 2 s.

Figure 11 shows the distributions of molecular gas mass, molecular gas mass fraction, the associated depletion timescales, SFRs, sSFRs, and offset from the MS. Overall, the distributions are similar. However, we do find the depletion timescales of Sy 2 galaxies are on average lower than Sy 1 galaxies ($p = 0.002$).

4.2.2. Line-of-sight Column Density and Molecular Gas

We next investigate the possible links between two completely independent probes of the (cold) gas content in our BAT AGN galaxies, which in principle originate from very different scales: the line-of-sight column density, N_{H} —as determined from detailed spectral modeling of the X-ray SEDs (Ricci et al. 2017), and the new molecular gas measurements.

In Figure 12 we plot N_{H} versus molecular gas mass, gas fraction, and depletion timescales both for individual (left panels) and binned (right panels) sources.

There are no significant trends between N_{H} and molecular gas mass. However, similar to the Seyfert 2 sample, a shorter depletion timescale is found for the absorbed systems ($p = 0.001$), which is most pronounced in the most absorbed systems ($\log(N_{\text{H}}/\text{cm}^{-2}) > 23.4$).

4.2.3. Intrinsic X-Ray Luminosity, Black Hole Mass, and Eddington Ratio

We next examine possible links between the molecular gas content of the BAT AGN hosts and key properties of the SMBHs that power their central engines. For this, we use measurements of intrinsic X-ray luminosities ($L_{2-10\text{ keV}}^{\text{in}}$; see Ricci et al. 2017), black hole mass (M_{BH}), and Eddington ratio

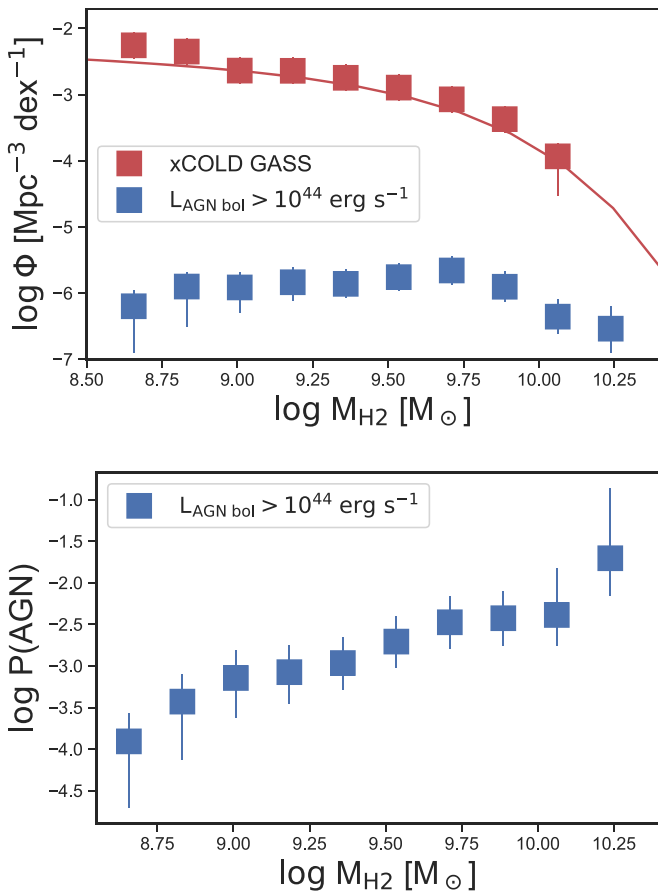


Figure 9. Top: The H_2 mass function for xCOLD GASS (see Figure 2, Fletcher et al. 2020) compared to galaxies hosting a BAT AGN ($L_{2-10 \text{ keV}}^{\text{in}} > 10^{41.8} \text{ erg s}^{-1}$ or $L_{\text{bol}} > 10^{44} \text{ erg s}^{-1}$). Error bars are based on Poisson statistics and include the number of nondetections in the lower limits. Only intervals with at least five sources per bin and with the majority detected are plotted. A red line indicates the best-fit Schechter function for xCOLD GASS. Bottom: the likelihood of a galaxy of a given molecular mass hosting an AGN, based on dividing the H_2 mass functions. The highest H_2 mass point (at $\log(M_{H_2}/M_{\odot}) = 10.23$) is based on an extrapolation of the best-fit Schechter function because of the limited numbers of sources in xCOLD GASS.

(L/L_{Edd} ; both from Koss et al. 2017), available through the BASS project.

In Figure 13 we plot $L_{2-10 \text{ keV}}^{\text{in}}$ versus the molecular gas mass, gas fraction, and depletion timescale. While there appears to be a slight increase in total molecular gas mass with X-ray luminosity, it is not statistically significant ($p = 0.10$) when comparing the higher luminosity half of our AGN to the lower luminosity half (above and below $\log(L_{2-10 \text{ keV}}^{\text{in}}/\text{erg s}^{-1}) = 43.2$, respectively). One area with a significant correlation is between the stellar mass and increased $L_{2-10 \text{ keV}}^{\text{in}}$ ($p = 0.001$, see Table 3).

Figure 14 shows the molecular gas properties compared to M_{BH} . No significant trends are found in any of the properties (molecular gas mass, gas fraction, or depletion timescale, SFR, sSFR, $\Delta(\text{MS})$). There is a significant trend between stellar mass and increased black hole mass, as expected ($p < 0.001$).

Finally, Figure 15 shows the molecular gas properties compared to L/L_{Edd} . The hosts of the highest Eddington ratio AGN ($\log L/L_{\text{Edd}} > -0.16$) have molecular gas masses that are significantly higher ($p = 0.037$) than hosts with the lowest Eddington ratio AGN, based on survival analysis. Similarly, the highest Eddington ratio AGN have significantly higher

($p = 0.042$) gas fractions than the lowest L/L_{Edd} ones. The gas depletion timescales, SFR, sSFR, $\Delta(\text{MS})$, and stellar mass show no statistically significant trends with Eddington ratio.

5. Discussion

Our results generally support the idea that rapidly growing, radiatively efficient AGN are fueled by a significant supply of cold gas, but this difference is concentrated in early and uncertain morphological types and more pronounced at higher stellar masses. These AGN host galaxies that are starkly different with higher gas fractions and SFRs than the population of quenched massive elliptical galaxies with undetectable star formation and molecular gas ($-12 < \log(\text{sSFR}/\text{yr}^{-1}) < -11$; Saintonge et al. 2017). There are also trends that support the idea that higher gas fractions increase the average normalized black hole growth rate (L/L_{Edd}).³⁶

5.1. Links to Coevolution and Stochastic Accretion

The global Eddington ratio and gas fraction correlation, as well as the increased likelihood of a galaxy with high molecular gas to host a luminous AGN, may be tracing an important part of SMBH and host-galaxy coevolution. High gas content may lead naturally to general correlations found in the SMBH and host (e.g., the correlations between SMBH mass and bulge properties; Kormendy & Ho 2013) and the similarity between the redshift evolution of star formation and SMBH growth (see the review of Heckman & Best 2014).

The correlations found between the Eddington ratio and both the total molecular gas mass and gas fraction (over the entire host galaxy) suggest that substantial cold gas may be concentrated in the nucleus of the galaxy. There is some evidence for this from Herschel FIR imaging of AGN hosts (Mushotzky et al. 2014; Lutz et al. 2018), which showed that a significant fraction of Herschel/PACS emission originates from compact sources, with typical scales of < 2 kpc. However, high-sensitivity interferometric observations of the central cores of AGN host galaxies are critical to confirm this scenario. Several ALMA campaigns are currently trying to pursue this challenging goal, including our own BASS-focused effort (T. Izumi et al. 2021, in preparation), but the samples are still rather small (< 40 AGN hosts). These high-resolution studies, which can overcome some of the huge difference in scales between the entire AGN galaxy studied here and the small scales of ultimate accretion are critical.

While statistically significant global trends and/or correlations ($p = 0.001 - 0.04$) are found in the large sample studied here ($N = 207$), it is crucial to stress that there is significant variation between individual AGN hosts, most likely driven by the stochasticity of both SMBH fuelling and the emergent AGN emission, and the galaxy-scale star formation processes (e.g., Hickox et al. 2014; Schawinski et al. 2015; Caplar & Tacchella 2019; Wang & Lilly 2019). This is similar to the result that when averaging over the full star-forming galaxy population, the average SMBH growth is correlated with SFR (e.g., Mullaney et al. 2012; Chen et al. 2013; Jones et al. 2019), as it is in the host galaxies of BAT AGN (Shimizu et al. 2017), although this correlation may be mainly linked to the host-galaxy stellar mass relation rather than star formation (Yang et al. 2017, 2018).

³⁶ Or, alternatively, that higher gas fractions are linked to shorter SMBH growth timescales, which scale inversely with L/L_{Edd} .

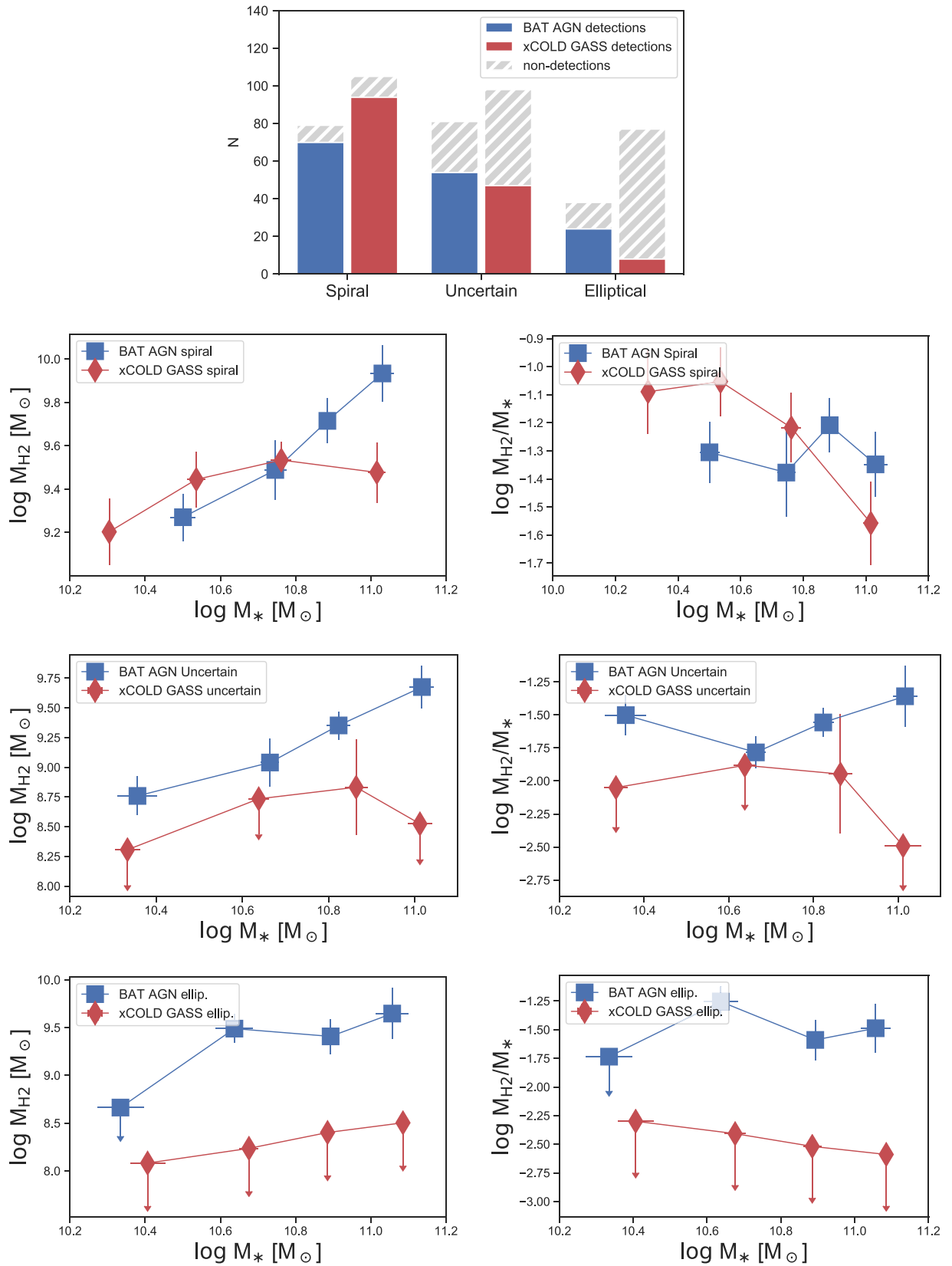


Figure 10. Links between molecular gas content and galaxy morphology for the BAT AGN galaxies and the xCOLD GASS inactive galaxy sample. Top left panel: distributions of galaxy morphology. For each sample and morphology class, gray bars indicate sources with CO(2–1) upper limits. The other panels show the median molecular gas mass and gas fraction vs. stellar mass for both AGN hosts and xCOLD GASS inactive galaxies, with either spiral, uncertain, or elliptical morphologies (second, third, and bottom row, respectively). Upper limits are shown when more than half the sample is upper limits. Note that more than half of all inactive galaxies with elliptical or uncertain morphologies have no robust CO detections.

Table 3
Summary of Median Parameters for Molecular Gas and Host Galaxy Parameters of AGN Galaxies

	$\log M_{\text{H}_2}$ $\log (M_{\odot})$	$\log M_{\text{H}_2}/M_{\odot}$	$\log t_{\text{dep}}(\text{H}_2)$ $\log (\text{yr})$	$\log \text{SFR}$ $\log (M_{\odot} \text{ yr}^{-1})$	$\log \text{sSFR}$ $\log(\text{yr}^{-1})$	$\Delta(\text{MS})$	$\log M_{*}$ $\log(M_{\odot})$
AGN Type							
Sy 1	$9.35^{+0.18}_{-0.08}$	$-1.47^{+0.04}_{-0.07}$	$9.02^{+0.06}_{-0.05}$	$0.33^{+0.14}_{-0.11}$	$-10.45^{+0.10}_{-0.07}$	$-0.19^{+0.09}_{-0.12}$	$10.80^{+0.07}_{-0.03}$
Sy 1.9	$9.37^{+0.43}_{-0.07}$	$-1.26^{+0.06}_{-0.22}$	$8.98^{+0.04}_{-0.15}$	$0.54^{+0.25}_{-0.15}$	$-10.25^{+0.22}_{-0.10}$	$0.00^{+0.16}_{-0.18}$	$10.79^{+0.09}_{-0.08}$
Sy 2	$9.36^{+0.13}_{-0.12}$	$-1.42^{+0.08}_{-0.23}$	$8.88^{+0.05}_{-0.07}$	$0.40^{+0.11}_{-0.16}$	$-10.32^{+0.12}_{-0.13}$	$-0.08^{+0.10}_{-0.19}$	$10.75^{+0.03}_{-0.07}$
$p < 0.05$			$p = 0.002$				
$\log(N_{\text{H}}/\text{cm}^{-2})$							
< 20.3	$9.31^{+0.21}_{-0.13}$	$-1.53^{+0.07}_{-0.11}$	$9.05^{+0.06}_{-0.09}$	$0.30^{+0.16}_{-0.11}$	$-10.47^{+0.09}_{-0.11}$	$-0.24^{+0.12}_{-0.10}$	$10.80^{+0.11}_{-0.04}$
20.3 – 22.5	$9.50^{+0.17}_{-0.15}$	$-1.43^{+0.11}_{-0.03}$	$9.02^{+0.02}_{-0.04}$	$0.39^{+0.10}_{-0.14}$	$-10.39^{+0.15}_{-0.06}$	$-0.15^{+0.15}_{-0.13}$	$10.79^{+0.08}_{-0.04}$
22.5 – 23.4	$9.35^{+0.16}_{-0.10}$	$-1.37^{+0.11}_{-0.07}$	$8.94^{+0.05}_{-0.09}$	$0.34^{+0.21}_{-0.21}$	$-10.21^{+0.09}_{-0.12}$	$-0.07^{+0.17}_{-0.11}$	$10.64^{+0.07}_{-0.05}$
>23.4	$9.32^{+0.28}_{-0.16}$	$-1.59^{+0.25}_{-0.12}$	$8.73^{+0.11}_{-0.07}$	$0.53^{+0.16}_{-0.18}$	$-10.27^{+0.15}_{-0.25}$	$-0.06^{+0.20}_{-0.21}$	$10.81^{+0.07}_{-0.04}$
$p < 0.05$			$p < 0.001$		$p = 0.034$		
$\log(L_{2-10 \text{ keV}}^{\text{in}}/\text{erg s}^{-1})$							
<42.8	$9.28^{+0.15}_{-0.07}$	$-1.44^{+0.13}_{-0.08}$	$8.99^{+0.05}_{-0.05}$	$0.28^{+0.19}_{-0.13}$	$-10.32^{+0.12}_{-0.14}$	$-0.18^{+0.20}_{-0.10}$	$10.60^{+0.08}_{-0.06}$
42.8 – 43.2	$9.34^{+0.19}_{-0.20}$	$-1.49^{+0.11}_{-0.08}$	$8.93^{+0.05}_{-0.09}$	$0.34^{+0.13}_{-0.21}$	$-10.40^{+0.12}_{-0.16}$	$-0.19^{+0.10}_{-0.17}$	$10.75^{+0.07}_{-0.06}$
43.2 – 43.4	$9.50^{+0.20}_{-0.15}$	$-1.34^{+0.13}_{-0.23}$	$8.96^{+0.19}_{-0.12}$	$0.55^{+0.15}_{-0.19}$	$-10.18^{+0.07}_{-0.17}$	$-0.03^{+0.16}_{-0.10}$	$10.78^{+0.11}_{-0.02}$
>43.4	$9.48^{+0.18}_{-0.21}$	$-1.47^{+0.04}_{-0.12}$	$8.88^{+0.14}_{-0.22}$	$0.43^{+0.20}_{-0.12}$	$-10.44^{+0.15}_{-0.08}$	$-0.18^{+0.17}_{-0.12}$	$10.88^{+0.11}_{-0.05}$
$p < 0.05$							$p = 0.001$
$\log(L/L_{\text{Edd}})$							
< -2	$9.29^{+0.13}_{-0.05}$	$-1.52^{+0.19}_{-0.11}$	$8.99^{+0.01}_{-0.05}$	$0.40^{+0.27}_{-0.11}$	$-10.35^{+0.16}_{-0.22}$	$-0.14^{+0.20}_{-0.19}$	$10.78^{+0.09}_{-0.08}$
-2 to -1.6	$9.35^{+0.13}_{-0.10}$	$-1.48^{+0.04}_{-0.20}$	$8.94^{+0.10}_{-0.03}$	$0.37^{+0.12}_{-0.17}$	$-10.42^{+0.13}_{-0.09}$	$-0.20^{+0.11}_{-0.11}$	$10.80^{+0.08}_{-0.05}$
-1.6 to -1.1	$9.50^{+0.20}_{-0.23}$	$-1.40^{+0.15}_{-0.13}$	$9.02^{+0.06}_{-0.14}$	$0.35^{+0.18}_{-0.11}$	$-10.35^{+0.13}_{-0.17}$	$-0.12^{+0.07}_{-0.18}$	$10.81^{+0.07}_{-0.07}$
> -1.1	$9.56^{+0.10}_{-0.22}$	$-1.43^{+0.11}_{-0.02}$	$8.88^{+0.07}_{-0.08}$	$0.50^{+0.18}_{-0.16}$	$-10.17^{+0.12}_{-0.16}$	$0.07^{+0.09}_{-0.22}$	$10.74^{+0.04}_{-0.14}$
$p < 0.05$	$p = 0.037$	$p = 0.042$					
$\log (M_{\text{BH}}/L_{\odot})$							
<7.4	$9.29^{+0.24}_{-0.18}$	$-1.43^{+0.14}_{-0.04}$	$8.91^{+0.05}_{-0.11}$	$0.33^{+0.16}_{-0.09}$	$-10.23^{+0.12}_{-0.15}$	$-0.09^{+0.24}_{-0.10}$	$10.55^{+0.12}_{-0.10}$
7.4 – 7.8	$9.45^{+0.18}_{-0.20}$	$-1.37^{+0.14}_{-0.10}$	$9.00^{+0.08}_{-0.03}$	$0.24^{+0.27}_{-0.09}$	$-10.30^{+0.15}_{-0.10}$	$-0.09^{+0.14}_{-0.15}$	$10.68^{+0.08}_{-0.03}$
7.8 – 8.1	$9.35^{+0.16}_{-0.05}$	$-1.53^{+0.08}_{-0.30}$	$8.98^{+0.05}_{-0.14}$	$0.34^{+0.25}_{-0.12}$	$-10.52^{+0.12}_{-0.15}$	$-0.28^{+0.13}_{-0.12}$	$10.88^{+0.02}_{-0.08}$
>8.1	$9.42^{+0.25}_{-0.15}$	$-1.47^{+0.13}_{-0.21}$	$8.93^{+0.06}_{-0.12}$	$0.55^{+0.08}_{-0.15}$	$-10.35^{+0.15}_{-0.22}$	$-0.06^{+0.11}_{-0.21}$	$10.91^{+0.04}_{-0.03}$
$p < 0.05$							$p < 0.001$

Note. Summary of median values for AGN host galaxies and the 1σ confidence limits based on a survival analysis using the KM estimator and the LIFELINES survival analysis package. A two sample survival analysis in time test is run between the two populations split in half between the highest and lowest values.

The ability to assess differences in star formation properties and offset from the MS complicated by systematic biases in measuring the SFR using different techniques in high stellar mass passive galaxies and AGN (and see Appendix B) and how “passive galaxies” are defined. However, the BAT AGN do have on average a higher fraction of massive spirals, bluer colors, more mergers, and more LIRGs (e.g., Koss et al. 2011a, 2013) than inactive galaxies, consistent with their higher molecular gas masses than inactive galaxies and typically higher SFRs than xCOLD GASS. We note that a previous study found that the BAT AGN predominantly lie below the MS of star-forming galaxies (but still well above passive galaxies; Shimizu et al. 2015) based on the Herschel observations, although we show that the BAT AGN galaxies are typically within the scatter of the MS. This is because there is significant difficulty establishing the low-redshift MS at high stellar masses ($\log(M_{*}/M_{\odot}) > 10.3$), such as studied here, in that there is potentially a flattening as well as increased scatter at high stellar masses (e.g., Popesso et al. 2019a, 2019b). Furthermore, the rarity of high-mass galaxies ($\log(M_{*}/M_{\odot}) > 11$) also contributes to this difficulty. This issue

will be further explored in a subsequent publication (T. Shimizu et al. 2021, in preparation).

5.2. AGN Feedback

Given the significant connection between gas-rich AGN host galaxies and black hole growth, the next question is to what extent AGN are able to suppress star formation activity throughout the host galaxy, or the infall of more (cold) gas onto the host. There is no significant evidence that the most luminous X-ray AGN galaxies have depletion timescales that are significantly shorter than lower luminosity AGN galaxies. This suggests that these AGN are not the primary drivers of quenching or evolution in the M_{*} -SFR plane. This could be because the measured “instantaneous” luminosities are weakly related due to the much longer timescales on which average stochastic accretion occurs. Large samples with hundreds of sources, such as the one studied here, combined with studies of the AGN history on longer timescales (e.g., Sartori et al. 2018), are crucial to overcome AGN variability and understand the role of AGN outbursts and feedback. Finally, high-sensitivity

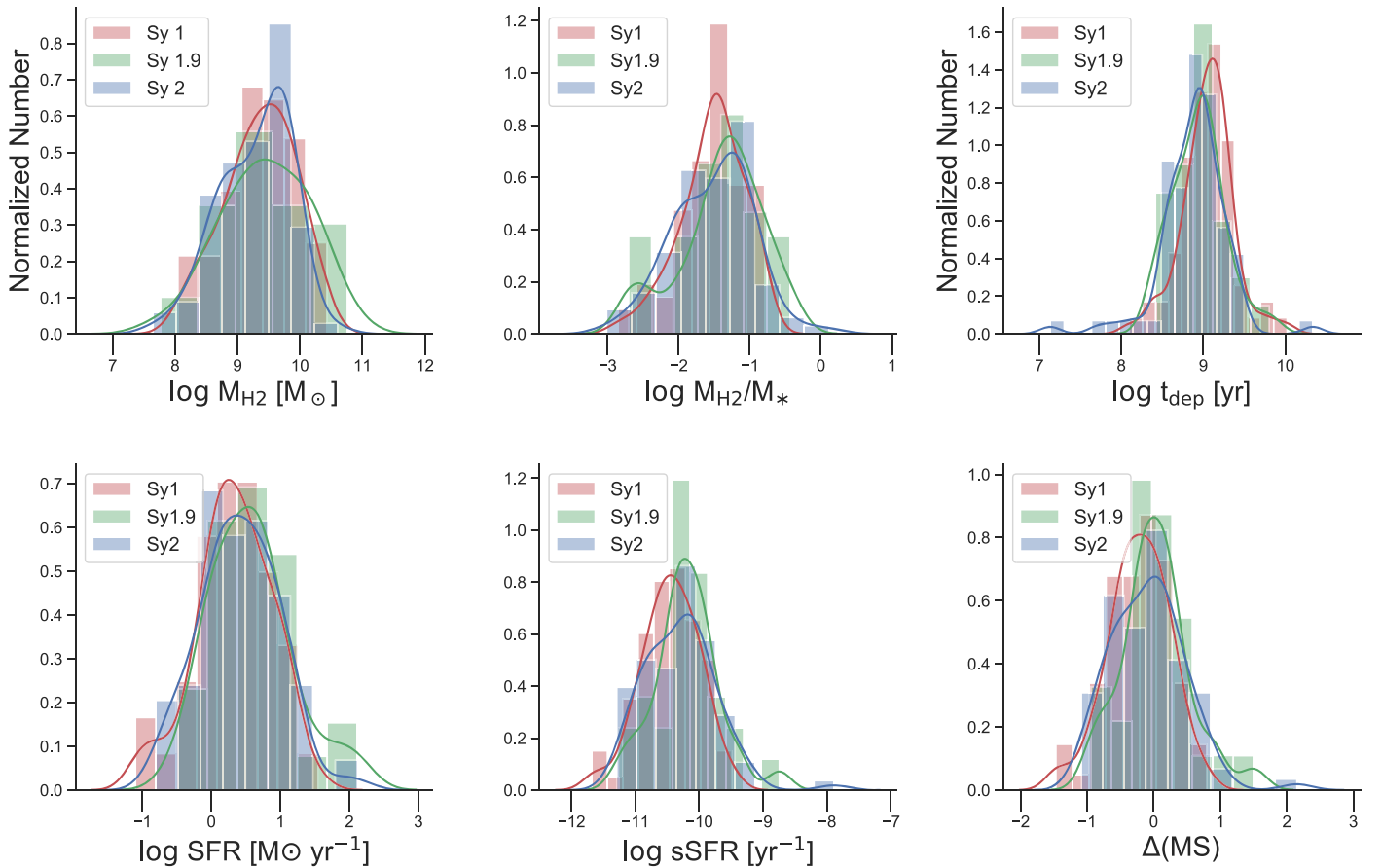


Figure 11. Molecular gas properties for different optical AGN galaxy subclasses. Distributions of molecular gas mass (upper left), gas fraction (upper right), depletion timescale (lower left), and sSFR (lower right), color-coded by the optical AGN classification. Sources that have both broad $\text{H}\alpha$ and $\text{H}\beta$ (red) are considered Sy 1 (e.g., type 1.0, 1.5, 1.8 etc.), sources with broad $\text{H}\alpha$ but only narrow $\text{H}\beta$ are Sy 1.9 (green), and finally, Sy 2 have only narrow Balmer lines. Lines represent kernel density estimates for the distributions. Seyfert 1.9 s are found to have higher gas fractions; otherwise, the distributions are statistically indistinguishable.

interferometric observations of the central cores of AGN host galaxies would also test whether signs of AGN feedback are present.

5.3. Gas-rich Ellipticals

The large amounts of molecular gas we find in BAT AGN that are hosted in elliptical galaxies is quite surprising and significant. Examples of some of the most gas-rich ellipticals in the BAT AGN galaxy sample are shown in Figure 16. We caution that some of these galaxies may be better classified as early types, as it is difficult to distinguish between true ellipticals and face-on lenticular hosts without deeper, higher quality imaging (e.g., from HST; see Appendix A)—as has been noted with Galaxy Zoo classifications (e.g., S0-SAs, Lintott et al. 2008). Importantly, ellipticals with significant molecular gas mass ($\log(M_{\text{H}_2}/M_{\odot}) > 9$) are quite rare among inactive galaxies. Of the 81 inactive massive ($\log(M_*/M_{\odot}) > 10.2$) ellipticals from xCOLD GASS, only 4% (3/81) have a significant amount of molecular gas. Similarly, the fraction of early-type galaxies with ($\log(M_{\text{H}_2}/M_{\odot}) > 9$) within the ATLAS3D sample is even lower, about 1% (3/260; Young et al. 2011).

In contrast, the majority (51%, or 21/41) of the elliptical hosts of BAT AGN are comparatively gas-rich (i.e., meeting the $\log(M_{\text{H}_2}/M_{\odot}) > 9$ criterion). Interestingly, the ATLAS3D survey found a significant trend between the molecular gas content and stellar specific angular momentum. Combined with our finding of

a high fraction of gas-rich ellipticals among BAT AGN hosts, this may suggest that the amount of galaxy angular momentum may be coupled to SMBH growth via stochastic accretion.

Given the lack of gas-rich early types among inactive galaxies, our results suggest that the many gas-rich early-type galaxies host luminous AGN. This is further supported by the most gas-rich early-type galaxy in xCOLD GASS (ID 3819) being excluded from the study due to hosting an AGN. Additionally, there is strong evidence that at least 2/3 early-type gas-rich galaxies in ATLAS3D host AGN based on radio data (Nyland et al. 2016). Further study is required to test this, however, because of the difference in volumes surveyed, and the rarity of both gas-rich early-type galaxies and of luminous AGN.³⁷

One obvious source of the additional gas in the massive galaxies is from mergers, which have already been shown to be significantly more common in BAT AGN hosts (e.g., Koss et al. 2010, 2011b, 2018). One might also expect an increase in the molecular-to-atomic gas ratio as measured from HI during the merger. The relatively high gas fractions of BAT AGN galaxies may explain the enhanced occurrence rate of dual AGN (Koss et al. 2012, 2018), which exceeds predictions from (low-redshift) simulations (Rosas-Guevara et al. 2016). As a specific example, looking at eight gas-rich BAT AGN galaxies with uncertain morphologies (Figure 17), 38% (3/8) are close

³⁷ The BAT AGN survey probed a volume of about $2 \times 10^7 \text{ Mpc}^3$, which is about 173 times larger than the ATLAS3D volume (Cappellari et al. 2011).

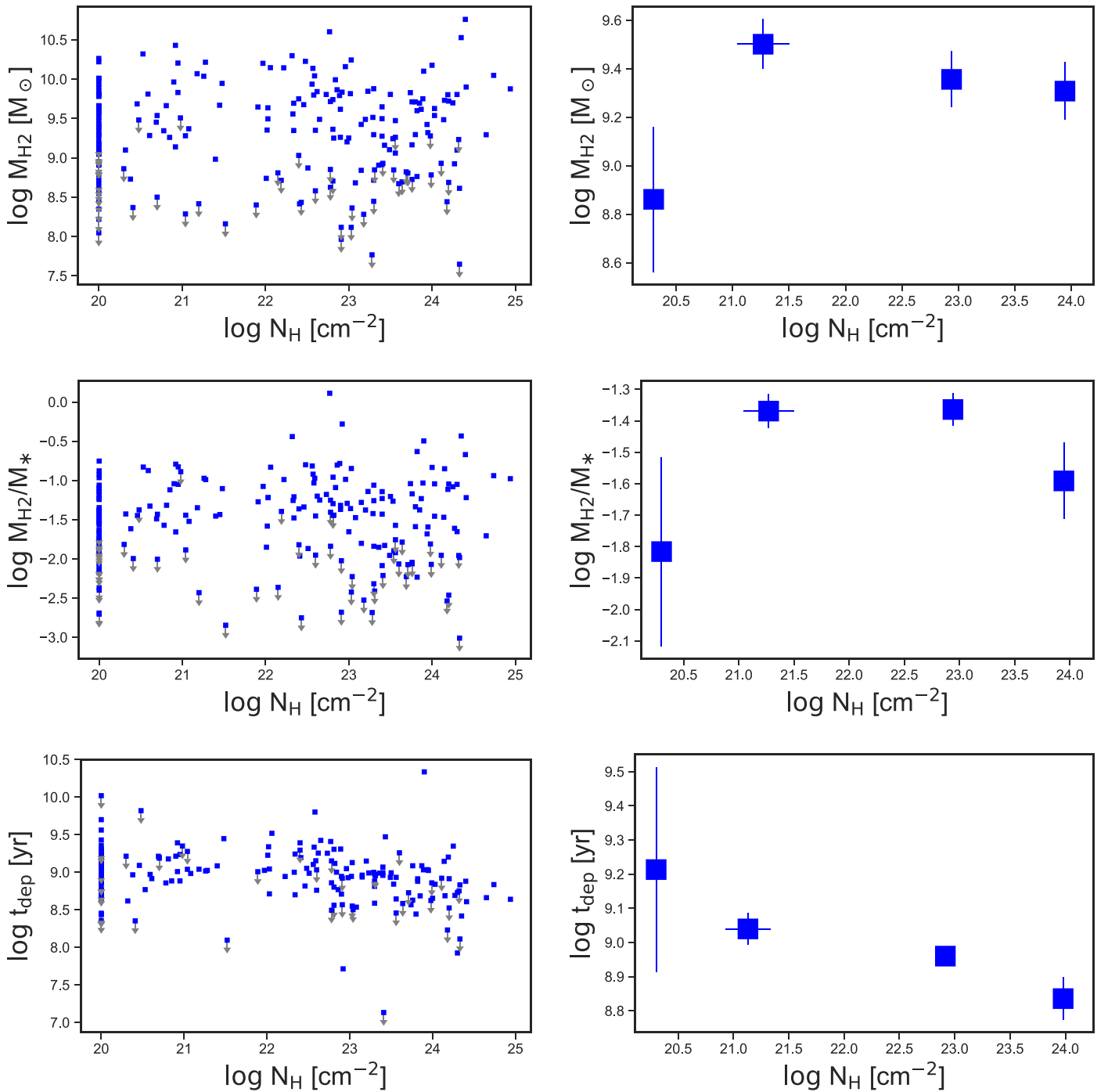


Figure 12. Links between molecular gas properties and the X-ray line-of-sight column density. The different panels show the molecular gas mass (top), molecular gas fraction (center), and depletion timescale (bottom). Fifty-two AGN have a column density consistent with a lower limit ($N_{\text{H}} = 10^{20} \text{ cm}^{-2}$). The scales of the median plots (right column) are smaller than those of the individual measurements (left column) to better highlight the subtle trends seen (or not seen).

mergers with separations between galaxy nuclei smaller than 3.5 kpc (Koss et al. 2018), whereas the rate among inactive galaxies for similarly close mergers is lower than 1%.

These observations may be able to measure the importance of externally acquired gas (e.g., from mergers and cold accretion). This was already clearly demonstrated in some inactive early-type galaxies (e.g., in the ATLAS3D sample; Davis et al. 2011), as the specific angular momentum of the gas is dramatically different from that of the stars. Early efforts studying dozens of the nearest BAT AGN galaxies are currently underway with ALMA (T. Izumi et al. 2021, in

preparation), in HI with the Australia Telescope Compact Array (I. Wong et al. 2021, in preparation), and for hundreds of BAT AGN galaxies with the Jansky Very Large Array (Smith et al. 2020).

5.4. AGN Obscuration

The finding that higher column density AGN galaxies ($\log(N_{\text{H}}/\text{cm}^{-2}) > 23.4$) and Seyfert 2 AGN galaxies are associated with lower depletion timescales suggests a connection to the gaseous environment of the nucleus. The higher

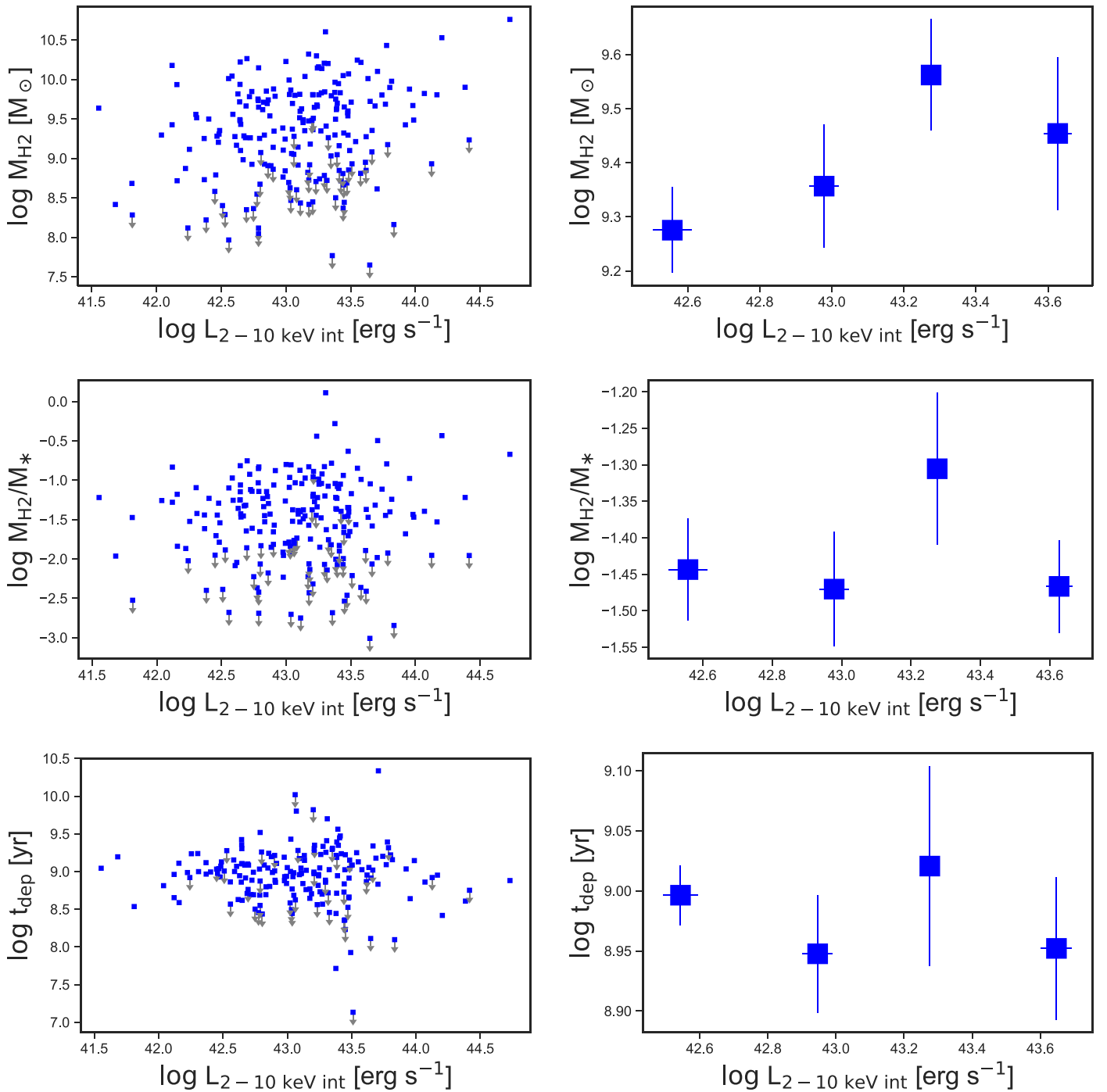


Figure 13. Molecular gas mass, gas fraction, and depletion timescale compared to the intrinsic X-ray luminosity (top, middle, and bottom panels, respectively).

column density AGN are also associated with higher sSFR. Obscured AGN may prefer hosts with more molecular gas centrally concentrated in the bulge associated with the torus that may be more prone to quenching than galaxy-wide molecular gas. The relationship between X-ray line-of-sight column density, the amount of molecular gas, stellar mass, and the inclination angle of the galaxies will likely allow one to further understand the galaxy-scale distribution of dusty, molecular gas, star formation, and the associated galaxy-scale obscuration (B. Strittmatter et al. 2021, in preparation). When also combined with higher resolution data, the closer (lower redshift) subset of the BAT AGN galaxies sample may provide a

unique ability to measure the amount of extended (0.1 – 1 kpc) molecular gas. This in turn will provide a template for interpreting the typical contribution of galaxy-scale contribution to the X-ray obscuration in distant AGN that is observed in deep surveys. At high redshift, the gas fractions are generally higher (Vito et al. 2014), and galaxy-scale obscuration is likely much more important for these surveys.

6. Summary and Conclusions

We reported observations of the $^{12}\text{CO}(2-1)$ emission line for 213 ultrahard-X-ray-selected AGN galaxies drawn from the Swift/BAT 70-month catalog. These data, obtained through

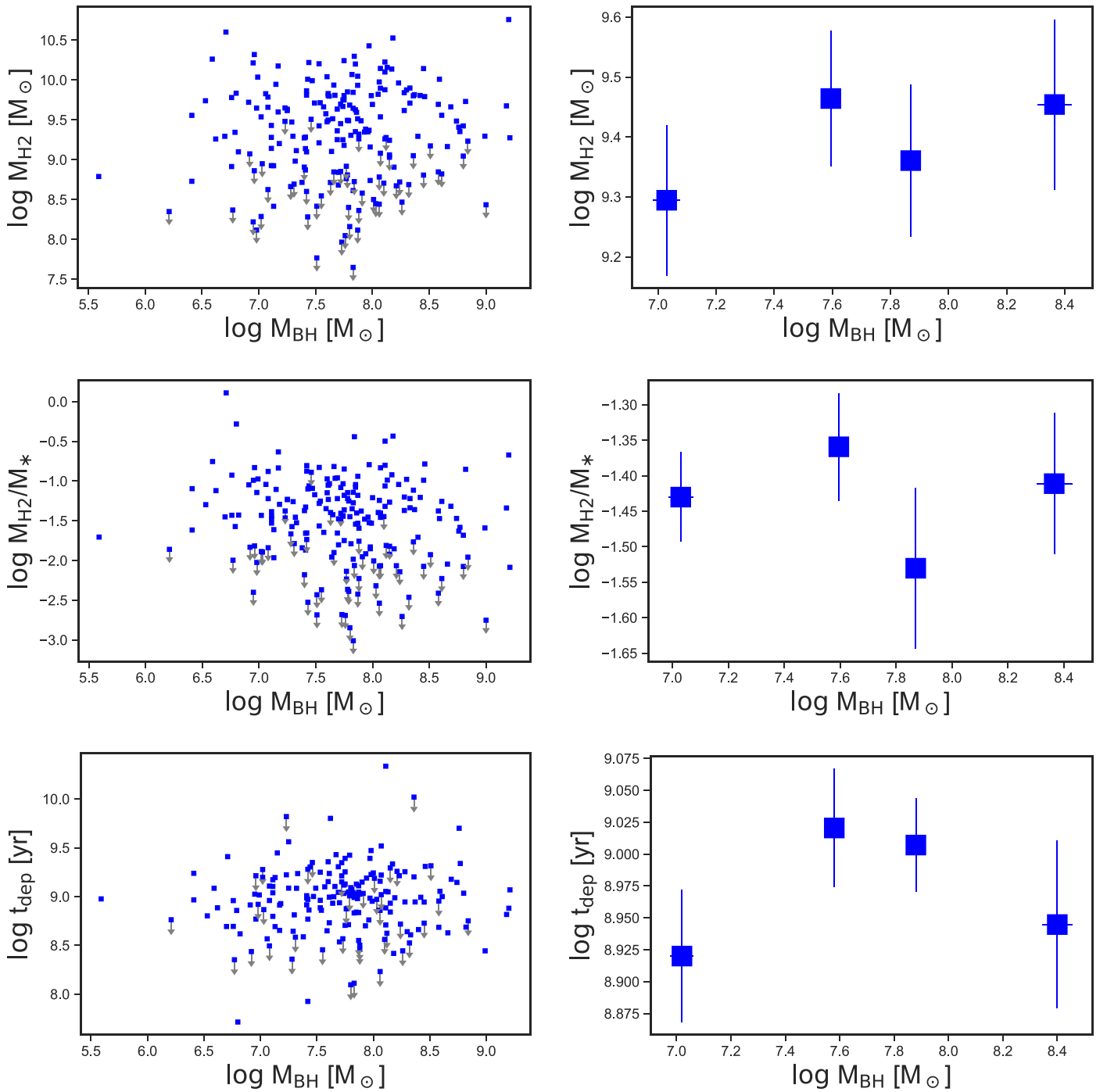


Figure 14. Molecular gas mass, gas fraction, and depletion timescale compared to the black hole mass (top, middle, and bottom panel, respectively). As in other figures, we show both individual measurements (left column of panels) and medians within bins (right panels). For presentation purposes, the scales of the median plots (right column) are smaller than in the left column to show sample differences.

large allocations of APEX and JCMT observing time, allowed us to reliably measure several key properties of the molecular gas in the hosts of these powerful AGN, including molecular gas mass and mass fraction, and depletion timescales. These were compared to similar measurements for a large comparison sample of inactive galaxies, drawn from the xCOLD GASS survey. Our analysis demonstrates that large ($N > 200$) samples of AGN galaxies with high-quality multiwavelength data and well-defined control samples are essential to understand the possible links between significant black hole growth

and the host-galaxy-scale molecular gas content. Our main findings are listed below.

1. AGN in massive galaxies ($\log(M_*/M_{\odot}) > 10.5$) tend to have more molecular gas and higher gas mass fractions than inactive galaxies matched in stellar mass ($p < 0.001$). The higher molecular gas content is related to AGN galaxies hosting a population of gas-rich early types with an order of magnitude more molecular gas, a smaller fraction of quenched, passive galaxies ($\sim 5\%$

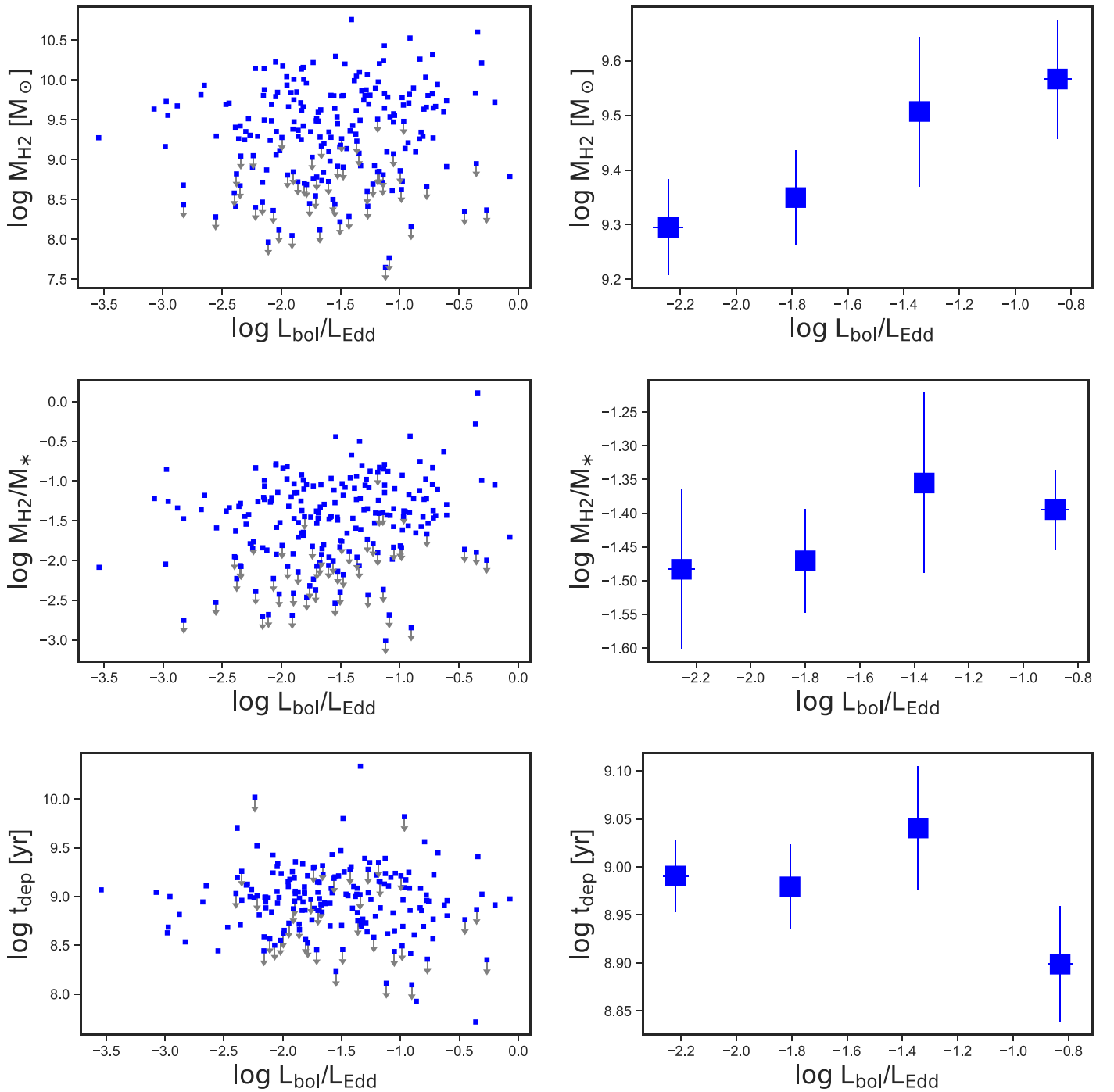


Figure 15. Molecular gas mass, gas fraction, and depletion timescale compared to the Eddington ratio (top, middle, and bottom panel respectively). As in other figures, we show both individual measurements (left column of panels) and medians within bins (right panels). There is a general increase in molecular gas mass and gas fraction with increasing L/L_{Edd} , while there is no trend with gas-depletion timescale. For presentation purposes, the scales of the median plots (right column) are smaller than in the left column to show sample differences.

- versus 49%), and a larger fraction of AGN galaxies on the MS of star formation compared to inactive galaxies.
- When matched in star formation, specific star formation, or offset from the MS of star formation, AGN galaxies are similar to inactive galaxies with respect to molecular gas and depletion timescales. There is no evidence that AGN feedback affects the host-galaxy cold molecular gas.

- The probability of hosting an AGN ($L_{2-10 \text{ keV}}^{\text{in}} > 10^{41.8} \text{ erg s}^{-1}$ or $L_{\text{bol}} > 10^{44} \text{ erg s}^{-1}$) is correlated with the total molecular gas and increases by a factor of ~ 10 – 100 between a molecular gas mass of $10^{8.7} M_{\odot}$ and $10^{10.2} M_{\odot}$.
- The hosts of AGN accreting at higher Eddington ratios have, on average, higher molecular gas masses ($p = 0.037$) and gas fractions ($p = 0.042$).

5. When matched by stellar mass and morphology, early-type AGN hosts show much higher molecular gas mass and gas fractions, by more than an order of magnitude, than inactive galaxies (e.g., $\log(M_{\text{H}_2}/M_{\odot}) = 9.58 \pm 0.07$ for AGN galaxies versus 8.36 ± 0.08 for inactive galaxies). This is related to the fact that the AGN galaxy sample lacks a significant number of massive and passive galaxies ($\log(\text{sSFR}/\text{yr}^{-1}) < -11$), which are common among the inactive ellipticals. AGN host galaxies are also more likely to be on the MS. Among spirals and uncertain morphologies, the difference in molecular gas content is significant for only the highest stellar masses ($\log(M_{*}/M_{\odot}) > 10.5$).
6. Higher column density AGN galaxies ($\log(N_{\text{H}}/\text{cm}^{-2}) > 23.4$) and Seyfert 2 AGN galaxies are associated with shorter depletion timescales. Obscured AGN may prefer hosts with more molecular gas centrally concentrated in the bulge that may be more prone to quenching than galaxy-wide molecular gas.

These results suggest that molecular gas has a critical role to play in black hole growth. Ultimately, a combination of interferometric CO observations (e.g., with ALMA or NOEMA), HI observations, and measurements of stellar dynamics from optical/near-IR integral-field spectroscopy at scales of hundreds of parsecs are critical to further interpret the excess of molecular gas in powerful AGN galaxies, and understand its role in fuelling SMBHs, and perhaps the way in which this SMBH growth may affect the host.

We acknowledge support from NASA through ADAP award NNH16CT03C and 80NSSC19K0749 (M.K.); the Israel Science Foundation through grant No. 1849/19 (B.T.); the Royal Society through the award of a University Research Fellowship (A.S.); ANID grants PIA ACT172033 (E.T.), Basal-CATA PFB-06/2007 and AFB170002 grants (E.T., F.E.B.), FONDECYT Regular 1160999, 1190818 (E.T., F.E.B.), and 1200495 (E.T., F.E.B.), and Millennium Science Initiative ICN12_009 (F.E.B.); the National Research Foundation of Korea (NRF-2020R1C1C1005462) (K.O.), the Japan Society for the Promotion of Science JSPS ID:17321 (K.O.); the ANID+PAI Convocatoria Nacional subvencion a instalacion en la academia convocatoria año 2017 PAI77170080 (C.R.); the UK Science and Technology Facilities Council through grants ST/P000541/1 and ST/T000244/1 (D.R.); and the Jet Propulsion Laboratory, California Institute of Technology, under a contract with NASA (D.S.). We acknowledge the work that Swift-BAT team has done to make this project possible. We acknowledge the help of Rozenn Boissay-Malaquin.

This publication is based on data acquired with the Atacama Pathfinder Experiment (APEX). APEX is a collaboration between the Max-Planck-Institut für Radioastronomie, the European Southern Observatory, and the Onsala Space Observatory. Based on observations collected at the European Organisation for Astronomical Research in the Southern Hemisphere under ESO programmes 198.A-0708(A), 0100.A-0384(A), 097.B-0757(A), 098.B-0152(A), 081.F-9405(A), and 091.F-9313(A) as well as Chilean programs C-097.F-9705A-2016, C-098.F-9700-2016, and C-0100.F-9715. The James Clerk Maxwell Telescope is operated by the East Asian Observatory on behalf of The National Astronomical Observatory of Japan; Academia Sinica Institute of Astronomy and Astrophysics; the Korea Astronomy and Space Science Institute; Center for

Astronomical Mega-Science (as well as the National Key R&D Program of China with No. 2017YFA0402700). Additional funding support is provided by the Science and Technology Facilities Council of the United Kingdom and participating universities in the United Kingdom and Canada. This project involved JCMT programs M11AH42C, M11BH35C, M12AH35C, M12BH03E, and M09BH34B. The Starlink software (Currie et al. 2014) is currently supported by the East Asian Observatory. This research made use of: the NASA/IPAC Extragalactic Database (NED), which is operated by the Jet Propulsion Laboratory, California Institute of Technology, under contract with the National Aeronautics and Space Administration and the SIMBAD database, operated at CDS, Strasbourg, France (Wenger et al. 2000).

Facilities: APEX, JCMT, PS1, Swift (BAT).

Software: astropy (Collaboration et al. 2013), APLpy (Robitaille & Bressert 2012), CIAO (v4.11, Fruscione et al. 2006), GILDAS (Pety 2005; Gildas Team 2013), lifelines (version 0.25.4, Davidson-Pilon et al. 2020), Matplotlib (Hunter 2007), Numpy (Harris et al. 2020), Sherpa (v4.12.1, Freeman et al. 2001; Burke & Laurino 2020), Starlink (Currie et al. 2014).

Appendix A Morphological Classification

Here we discuss issues related to morphological classification using ground-based data even for nearby galaxies. Examples of galaxy morphologies from the sample for elliptical morphologies can be found in Figure 16, for uncertain morphologies in Figure 17, and for spiral morphologies in Figure 18.

We primarily investigate the elliptical classification because the excess of molecular gas among AGN galaxies compared to inactives was most significant. Galaxy Zoo morphologies, which are used in both samples, are known to include some of the S0-Sa continuum (Lintott et al. 2008). There is also a bias in comparing between samples that the tendency is that a fainter, higher redshift galaxy will be more likely classified as an elliptical due to the difficulty of identifying faint spiral arms.

Our study contains 34% (73/213) of galaxies with only DSS images in the southern hemisphere ($\delta < -30^\circ$) which may, due to their poorer quality imaging, have some bias to elliptical morphologies. Of these, 19% (14/73) have elliptical morphologies. However, we do not find that these galaxies with DSS imaging have a significantly higher fraction of ellipticals than the majority with SDSS or PS1 imaging, where the fraction is 20% (28/140), suggesting that this is not a significant issue.

We then focus our study on the 13 BAT AGN galaxies with the most molecular gas ($\log(M_{\text{H}_2}/M_{\odot}) > 9.5$), which is higher than any of the elliptical galaxies either from xCOLD GASS or the ATLAS sample. First, we use Hyperleda to study whether morphological classifications from other publications are consistent with ours. We find that of the 13 BAT AGN galaxies, 9 are classified as elliptical, 3 as S0, and 1 as SA.

Lower surface brightness features such as spiral disks can be found with higher quality imaging such as from the HST (e.g., Ellis et al. 2000), as well as features such as nuclear spirals (e.g., Martini & Pogge 1999; Martini et al. 2003a, 2003b), which are only resolved with high spatial resolution imaging.

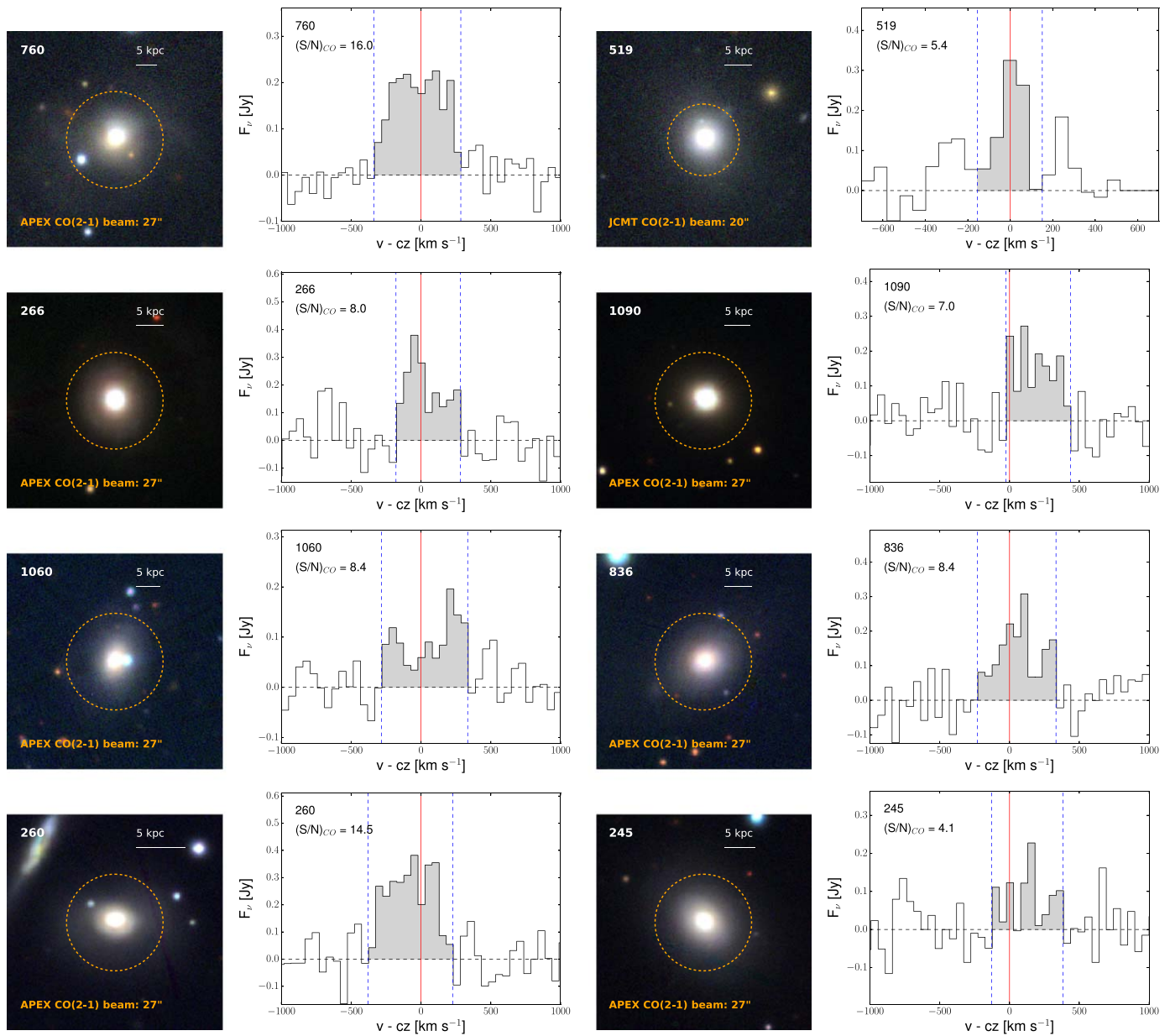


Figure 16. Pan-STARRS $1' \times 1'$ example gri images of the BAT AGN sample for galaxies classified as elliptical with some of the highest molecular gas masses. The galaxies are sorted from largest (upper left, ID = 760, $\log M_{\text{H}_2} = 10.27 M_{\odot}$) to smallest (bottom right, ID = 102, $\log M_{\text{H}_2} = 9.53 M_{\odot}$) in molecular gas content from left to right and top to bottom. All of these galaxies have more molecular gas than any of the 81 inactive massive ($\log M_{*} > 10.2 M_{\odot}$) ellipticals from xCOLD GASS.

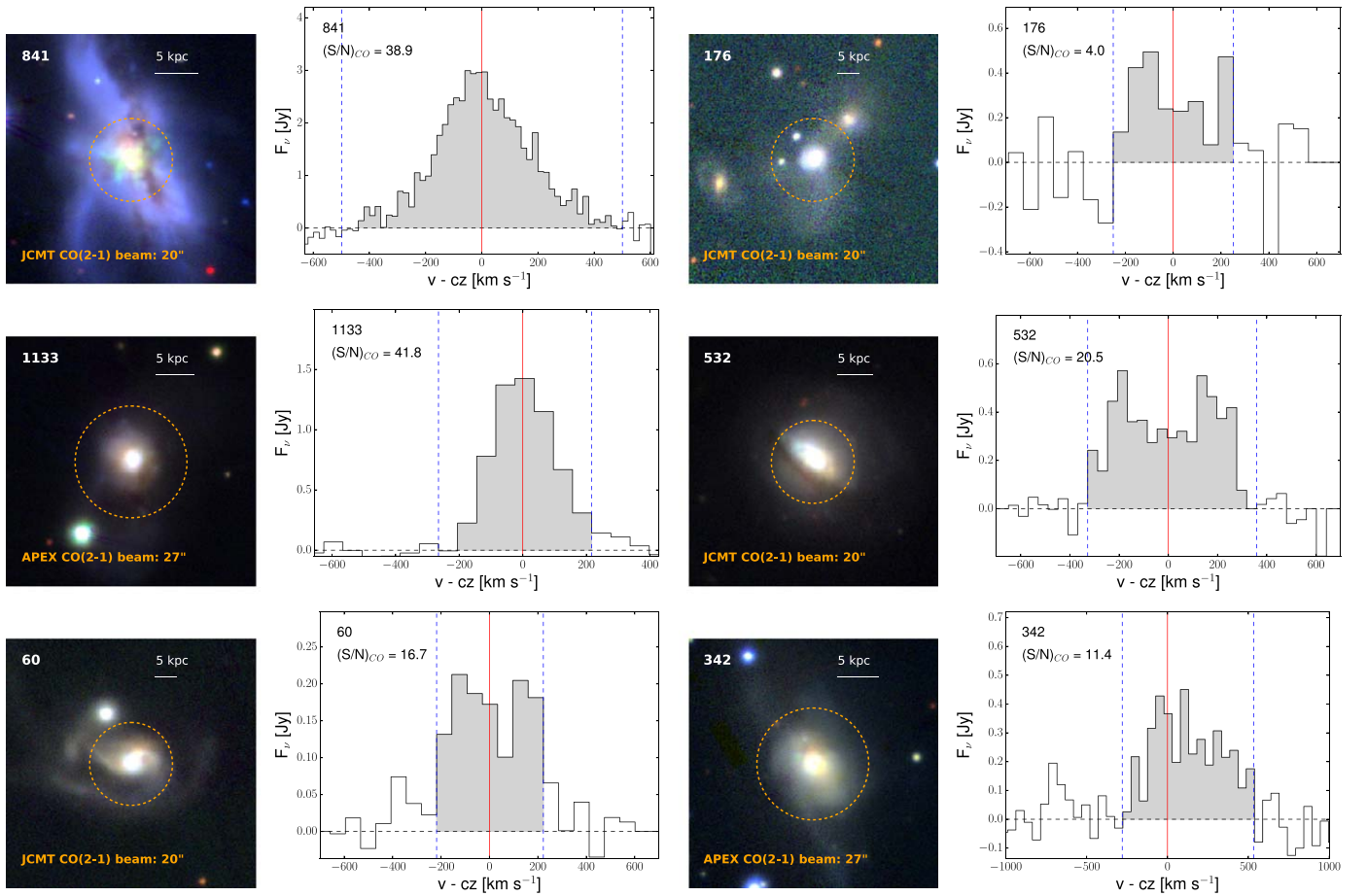


Figure 17. Pan-STARRS $1' \times 1'$ example *gri* images of the BAT AGN sample for galaxies classified as uncertain with some of the highest molecular gas masses. The galaxies are sorted from largest (upper left, ID = 841, $\log(M_{\text{H}_2}/M_{\odot}) = 10.76$) to smallest (bottom right, ID = 342, $\log(M_{\text{H}_2}/M_{\odot}) = 10.01$) in molecular gas content from left to right and top to bottom. All galaxies in the top row have more molecular gas than any of the 105 inactive massive ($\log(M_{\text{H}_2}/M_{\odot}) > 10.2$) uncertain galaxy morphologies from xCOLD GASS.

We found that 4/13 sources have optical HST imaging. Of these, 1 was classified as an elliptical (Mrk 509), 2 as an SA (Fairall 49 and ESO 323-77), and finally, 1 as a peculiar/SB system due to a nuclear spiral (Ark 120) based on previous studies (Malkan et al. 1998; Bentz et al. 2009).

Among the xCOLD GASS inactive elliptical sample, there are eight detections with much lower molecular gas masses ($\log(M_{\text{H}_2}/M_{\odot}) = 8.5\text{--}9.3$). Four are reported as elliptical in

Hyperleda, and four as S0-SAs. No optical HST images exist for the sample.

In summary, we find that the elliptical sample with gas detections includes a significant fraction of lenticular systems in both BAT AGN galaxies and the inactive galaxies. Further large studies of morphology with the HST would be necessary to investigate how common weak spiral arms or nuclear spirals are in these systems.

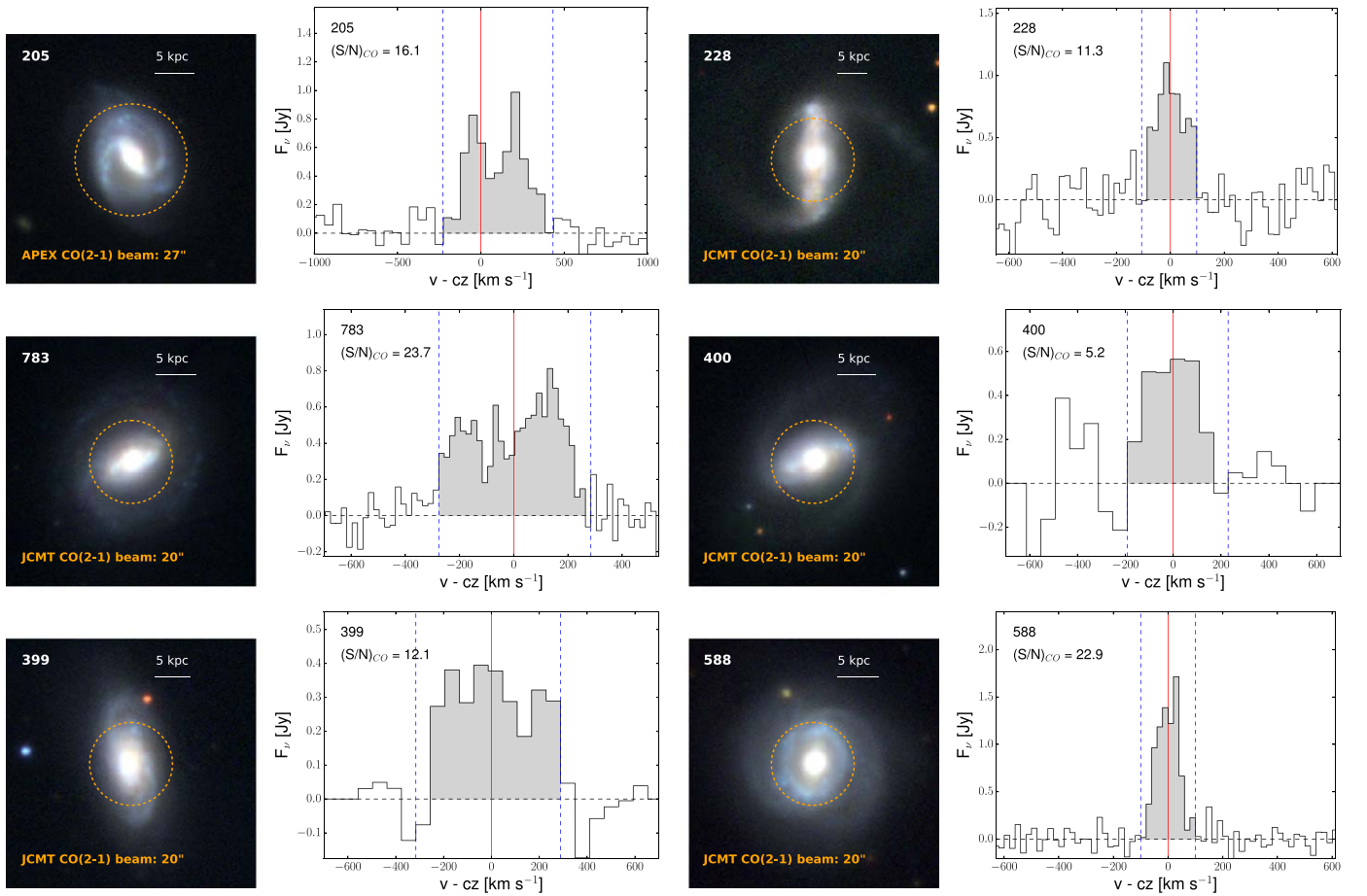


Figure 18. Pan-STARRS $1' \times 1'$ example *gri* images of the BAT AGN sample for galaxies classified as spiral with some of the highest molecular gas masses. The galaxies are sorted from largest (upper left, ID = 205, $\log(M_{\text{H}_2}/M_{\odot}) = 10.11$) to smallest (bottom right, ID = 588, $\log(M_{\text{H}_2}/M_{\odot}) = 9.93$) in molecular gas content from left to right and top to bottom.

Appendix B

Uncertainty in Derived Parameters for Inactive Galaxies and AGN Galaxies

The derived parameters (stellar mass, gas-depletion timescales, etc.) for inactive and AGN host galaxies require a few assumptions because some of the parameters are derived differently because of the difficulty dealing with AGN contamination of the multiwavelength emission. The stellar masses are both computed using SED fitting, but there is some uncertainty in the AGN emission. In general, the results in this paper are more significant than the likely scatter or possible offsets, however.

First, for the stellar mass measurements, 18 BAT AGN overlap with the Max Planck Institute for Astrophysics/Johns Hopkins University (MPA/JHU) catalog, which was used for xCOLD GASS stellar mass measurements. The agreement in stellar masses for these AGN is good, with the BAT AGN stellar masses somewhat lower than those in the catalog ($\log(M_*/M_{\odot}) = -0.07 \pm 0.15$).

Second, we have assumed the CO (2-1) can be reliably converted into the CO(1-0) assuming a conversion of 0.79 ± 0.03 , which was derived from xCOLD GASS. For the CO(2-1), Lamperti et al. (2017) examined the CO(3-2) and CO(1-0) for these AGN galaxies compared to xCOLD GASS inactive galaxies and found no significant offset, so we would not expect an offset in CO(2-1). Shangquan et al. (2019)

studied a sample of 15 Palomar-Green quasars and found no offset in CO (2-1) to CO (1-0) either.

One area where there may be systematic offsets is the derivation of SFR and hence depletion timescales that are derived from the SED fitting of the IR (Shimizu et al. 2017; Ichikawa et al. 2019). There is also some uncertainty in the level to which the AGN contaminates the FIR emission that was used to estimate the SFR after SED fitting to remove the AGN contribution (e.g., Shimizu et al. 2017; Ichikawa et al. 2019), particularly in studies of luminous systems, which might affect depletion timescales. In xCOLD GASS, the SFR estimates are from an average of near-UV, optical, and mid-IR fitting (Janowiecki et al. 2017) as well as from the MPA/JHU catalog from optical measurements. For the purpose of this study, we used the SED fitting SFR measurements from xCOLD GASS to better match the Herschel-based SED fits. For emission-line galaxies, the SFRs of xCOLD GASS were found to be in very good agreement with H-alpha (0.2 dex scatter with 0.01 offset across three orders of mag), which has been shown to be in good agreement with the FIR emission, but with some scatter consistent with previous studies (see e.g., Kennicutt & Evans 2012, for review).

In order to better understand the offsets, we crossmatched the BAT AGN galaxies with measurements from either the MPA/JHU catalog or GALEX–SDSS–WISE Legacy Catalog version 2 (GSWLC-2; Salim et al. 2018). GSWLC-2

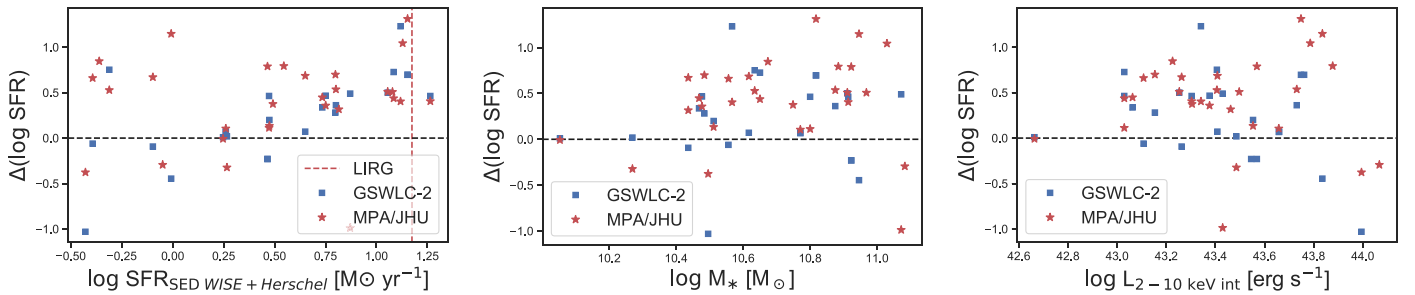


Figure 19. Comparison between the SFR derived measurements for the same BAT AGN galaxies using different studies. The offset, $\Delta(\text{SFR})$, is defined as the difference on a logarithmic scale between the measured SFR between studies. The left panel shows the $\Delta(\text{SFR})$ as compared to the SFR, with a dashed line indicating the boundary with LIRGs. The middle panel shows the offset with stellar mass. Finally, the right panel shows the offset with AGN X-ray luminosity.

determines SFRs from joint UV+optical+mid-IR SED fitting along with CIGALE (Noll et al. 2009). Because only a small number of BAT AGN galaxies are in the SDSS footprint, we used the full sample of BAT AGN galaxies (e.g., including those unobserved, as shown in Figure 1), limited to BAT AGN where the SFR was detected rather than a limit. This left us with a sample of 32 BAT AGN galaxies with overlapping SFR measurements for the same AGN galaxies (Figure 19).

We found that the Herschel derived SED SFRs in our studies were typically significantly higher, with the median offset and 1σ confidence as $0.28_{0.22}^{+0.18}$ dex for GSWLC-2 and $0.45_{0.07}^{+0.08}$ dex for the MPA/JHU, respectively. The SFR offsets are consistent with previous studies of AGN and massive galaxies when measured with Herschel (e.g., see Figure 12, Rosario et al. 2016). The AGN galaxies with the highest offsets tended to be those near the LIRG boundary, with some of the highest IR luminosities in the local universe in the sky, indicating that some of this offset might be in systems with much obscured star formation. If the evolved stars significantly contribute to the dust heating measured in the FIR, causing an overestimate of the IR-based SFR, we might expect a correlation with stellar mass, which we do not find. Finally, we do not see any correlation in the offsets with AGN X-ray luminosity, which we might expect if the AGN contribution to the IR were incorrectly subtracted.

In xCOLD GASS the SFR estimates which we directly compare to are from Janowiecki et al. (2017), which itself is somewhat above the MPA/JHU ($\Delta(\text{SFR}) = 0.28$) and GSWLC-2 ($\Delta(\text{SFR}) = 0.21$ dex), so it is possible that some of these offsets between AGN galaxies and xCOLD GASS cancel each other. In summary, systematic offsets in SFR measurements between AGN and inactive galaxies and FIR versus UV-optical-mid-IR may limit our ability to measure small differences (≈ 0.3 dex) in gas-depletion times, star formation properties, and offset from the MS. In the current sample, the evidence suggests that the Herschel-based measurements may better capture obscured star formation, however.

These issues will be further explored in a subsequent paper studying the combined results from this paper and a large IRAM program ($N = 129$ BAT AGN galaxies), which has the benefit of both a larger sample size and an overlap for 56 of the AGN galaxies from the APEX and JCMT data presented here (T. Shimizu et al. 2021, in preparation). This paper will perform a full UV-optical-mid-IR fitting.

Appendix C Beam-correction Methods

We have used somewhat different beam-correction methods for the AGN and inactive galaxies. Because the galaxies have not been mapped in CO beyond the primary beam, the critical issue is what other imaging wavelength best represents the CO scale lengths to provide the most accurate correction. As discussed in the text, the xCOLD GASS sample used a combination of simulations and the g -band surface brightness. The BAT AGN galaxy sample primarily used PACS $160\ \mu\text{m}$ surface brightness, but when these were not available, it used the K_s -band surface brightness.

The effect of using different imaging for the correction of the CO beam is still little understood, although the literature suggests that FIR (e.g., $70\ \mu\text{m}$ or $160\ \mu\text{m}$) tracers are most effective. Leroy et al. (2008) found that in spirals, the star formation efficiency ($\text{SFE} = \text{SFR}/M_{\text{H}_2}$) based on H_2 is nearly constant at $800\ \text{pc}$ resolutions, compared to $3.6\ \mu\text{m}$ data. However, when the interstellar medium is predominantly H I, the SFE drops with a smaller scale length. A further study by Schruba et al. (2011) used IRAM to study CO emission in 33 nearby spirals down to very low intensities. They found a tight linear relationship between $24\ \mu\text{m}$ and $70\ \mu\text{m}$ that does not show any notable break between regions that are dominated by molecular gas or H I. The correlation was much weaker and the scatter much larger for the far-UV and $\text{H}\alpha$ emission. Corbelli et al. (2012) found that the CO (1–0) flux correlates tightly and linearly with FIR fluxes observed by Herschel, especially with the emission at 160 , 250 , and $350\ \mu\text{m}$. Bourne et al. (2013) found that the correlation between CO (3–2) is strongest at $100\ \mu\text{m}$, compared to longer or shorter Herschel wavelengths, but that CO (2–1) may be more closely related to colder dust at longer wavelengths. Casasola et al. (2017) studied 18 face-on spiral galaxies and fit the surface-brightness profiles, finding that the scale lengths at $160\ \mu\text{m}$ are somewhat smaller than at $3.6\ \mu\text{m}$ (0.9) and the $70\ \mu\text{m}$ is smaller still than the $3.6\ \mu\text{m}$ (0.84). The total H_2 scale length from CO is found on somewhat smaller scales than the $70\ \mu\text{m}$ (0.85), $160\ \mu\text{m}$ (0.77), and $0.5\ \mu\text{m}$, which is similar to the g -band central wavelength used for xCOLD GASS (0.65).

The median beam correction for all the BAT AGN galaxies is 1.33, which is higher by 16% than the xCOLD GASS survey (1.15), although the BAT AGN galaxies are at lower redshifts and higher stellar masses, so some offset is naturally expected. The average K -band effective radius (R_{k20}) for the BAT AGN

galaxy sample is $21''7$, and for xCOLD GASS, it is $15''7$, indicating the BAT AGN host galaxies are on average 38% larger on the sky than the xCOLD GASS comparison sample. The ratio of effective radius to HPBW is on average 0.86 for BAT AGN host galaxies and 0.71 for xCOLD GASS inactives, indicating the BAT AGN galaxies are on average 20% larger than the beam size. We then compare the ratio of the beam correction between BAT AGN and inactive galaxies based on the average ratio of the beam correction to K-band effective radius (R_{k20}) because presumably, a larger galaxy would have a larger beam correction. We find the BAT AGN galaxy beam correction per arcsecond effective radius is on average slightly lower (0.0698 ± 0.002) than in inactive galaxies (0.0724 ± 0.001).

Appendix D Measuring CO Using Integrated Emission versus Profile Fitting

In the catalog we have provided measurements by integrating the line flux, so that we can robustly compare with xCOLD GASS using the exact same measurement techniques. For upper limits in the AGN galaxy sample, we have also assumed the exact same width (300 km s^{-1}) as xCOLDGASS, which matches the median width of the detected BAT sample well ($w_{50} = 295 \text{ km s}^{-1}$).

We have also provided catalog measurements using profile fitting with Gaussians, although they are not used in the sample analysis. In Figure 20 we provide a comparison of the flux of the integrated fitting method compared to the line fitting methods for detected sources. There is good agreement with the mean ratio between the fluxes of 1.05 ± 0.10 of the integrated flux to the flux from profile fitting with Gaussians.

Eleven sources are detected using integrated measurements with an S/N between 3.1 and 5.9, but they are nondetections when a profile fit is used ($S/N < 3$). One source, ID = 586 is at $S/N = 1.6$ with a profile fit, and the remaining sources are between $S/N = 2.2$ – 2.7 . Of these, 6/11 were reobserved with IRAM (T. Shimizu et al. 2021, in preparation), and all six were confirmed detections ($S/N = 3.4$ – 18.1).

The line profiles and a comparison with IRAM observations will be further studied in T. Shimizu et al. (2021, in preparation), with a large number of northern hemisphere BAT AGN galaxies, ensuring the higher sensitivity required for this type of analysis.

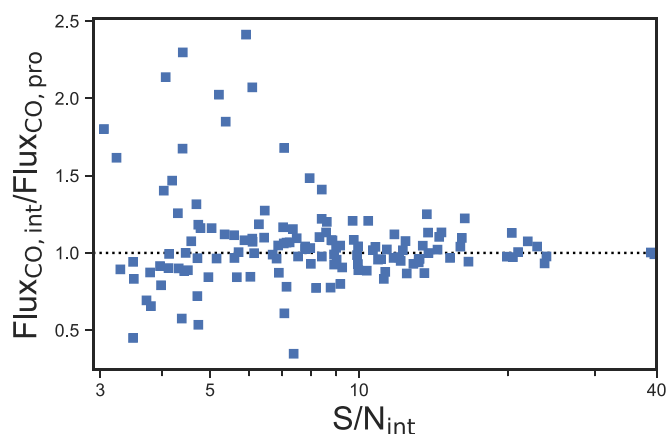


Figure 20. Comparison between the fluxes from integrating the total CO emission vs. profile line fitting with Gaussians. Other than at low S/N ($3 < SN < 5$), there is good agreement between the methods.

ORCID iDs

Michael J. Koss <https://orcid.org/0000-0002-7998-9581>
 Benjamin Strittmatter <https://orcid.org/0000-0002-7606-3679>
 Isabella Lamperti <https://orcid.org/0000-0003-3336-5498>
 Taro Shimizu <https://orcid.org/0000-0002-2125-4670>
 Benny Trakhtenbrot <https://orcid.org/0000-0002-3683-7297>
 Amelie Saintonge <https://orcid.org/0000-0003-4357-3450>
 Ezequiel Treister <https://orcid.org/0000-0001-7568-6412>
 Claudia Cicone <https://orcid.org/0000-0003-0522-6941>
 Richard Mushotzky <https://orcid.org/0000-0002-7962-5446>
 Kyuseok Oh <https://orcid.org/0000-0002-5037-951X>
 Claudio Ricci <https://orcid.org/0000-0001-5231-2645>
 Daniel Stern <https://orcid.org/0000-0003-2686-9241>
 Tonima Tasnim Ananna <https://orcid.org/0000-0001-8211-3807>
 Franz E. Bauer <https://orcid.org/0000-0002-8686-8737>
 George C. Privon <https://orcid.org/0000-0003-3474-1125>
 Rudolf E. Bär <https://orcid.org/0000-0001-5481-8607>
 Carlos De Breuck <https://orcid.org/0000-0002-6637-3315>
 Kohei Ichikawa <https://orcid.org/0000-0002-4377-903X>
 Meredith C. Powell <https://orcid.org/0000-0003-2284-8603>
 David Rosario <https://orcid.org/0000-0002-0001-3587>
 David B. Sanders <https://orcid.org/0000-0002-1233-9998>
 Kevin Schawinski <https://orcid.org/0000-0001-5464-0888>
 Li Shao <https://orcid.org/0000-0003-2015-777X>
 C. Megan Urry <https://orcid.org/0000-0002-0745-9792>
 Sylvain Veilleux <https://orcid.org/0000-0002-3158-6820>

References

- Accurso, G., Saintonge, A., Catinella, B., et al. 2017, *MNRAS*, 470, 4750
 Alonso-Herrero, A., García-Burillo, S., Pereira-Santaella, M., et al. 2019, *A&A*, 628, A65
 Ananna, T. T., Treister, E., Urry, C. M., et al. 2020, *ApJ*, 889, 17
 Antonucci, R. 1993, *ARA&A*, 31, 473
 Barthelmy, S. D., Barbier, L. M., Cummings, J. R., et al. 2005, *SSRv*, 120, 143
 Baumgartner, W. H., Tueller, J., Markwardt, C. B., et al. 2013, *ApJS*, 207, 19
 Bentz, M. C., Peterson, B. M., Netzer, H., Pogge, R. W., & Vestergaard, M. 2009, *ApJ*, 697, 160
 Bertram, T., Eckart, A., Fischer, S., et al. 2007, *A&A*, 470, 571
 Best, P. N., & Heckman, T. M. 2012, *MNRAS*, 421, 1569
 Bischetti, M., Piconcelli, E., Feruglio, C., et al. 2019, *A&A*, 628, A118
 Bolatto, A. D., Warren, S. R., Leroy, A. K., et al. 2013, *Natur*, 499, 450
 Boselli, A., Cortese, L., & Boquien, M. 2014, *A&A*, 564, A65
 Bothwell, M. S., Wagg, J., Cicone, C., et al. 2014, *MNRAS*, 445, 2599
 Bourne, N., Dunne, L., Bendo, G. J., et al. 2013, *MNRAS*, 436, 479
 Brusa, M., Cresci, G., Daddi, E., et al. 2018, *A&A*, 612, A29
 Burke, D., & Laurino, O. 2020, sherpa/sherpa: Sherpa v4.12.1, Zenodo, doi: 10.5281/zenodo.3944985
 Caplar, N., & Tacchella, S. 2019, *MNRAS*, 487, 3845
 Cappellari, M., Emsellem, E., Krajnović, D., et al. 2011, *MNRAS*, 413, 813
 Casasola, V., Cassarà, L. P., Bianchi, S., et al. 2017, *A&A*, 605, A18
 Chen, C.-T. J., Hickox, R. C., Alberts, S., et al. 2013, *ApJ*, 773, 3
 Cicone, C., Bothwell, M., Wagg, J., et al. 2017, *A&A*, 604, A53
 Cicone, C., Severgnini, P., Papadopoulos, P. P., et al. 2018, *ApJ*, 863, 143
 Cimatti, A., Brusa, M., Talia, M., et al. 2013, *ApJL*, 779, L13
 Collaboration, A., Robitaille, T. P., Tollerud, E. J., et al. 2013, *A&A*, 558, A33
 Combes, F. 2018, *A&ARv*, 26, 5
 Corbelli, E., Bianchi, S., Cortese, L., et al. 2012, *A&A*, 542, A32
 Currie, M. J., Berry, D. S., Jenness, T., et al. 2014, in ASP Conf. Series 485, Astronomical Data Analysis Software and Systems XXIII, ed. N. Manset & P. Forshay (San Francisco, CA: ASP), 391
 Dasyra, K. M., & Combes, F. 2012, *A&A*, 541, L7
 Davidson-Pilon, C., Kalderstam, J., Jacobson, N., et al. 2020, CamDavidsonPilon/Lifelines, v0.25.4, Zenodo, doi: 10.5281/zenodo.4002777
 Davis, T. A., Bureau, M., Young, L. M., et al. 2011, *MNRAS*, 414, 968
 de Vaucouleurs, G., de Vaucouleurs, A., Corwin, H. G., et al. 1995, *yCat*, 7155, 0

- Ellis, R. S., Abraham, R. G., Brinchmann, J., & Menanteau, F. 2000, *A&G*, **41**, 10
- Feruglio, C., Maiolino, R., Piconcelli, E., et al. 2010, *A&A*, **518**, L155
- Fiore, F., Feruglio, C., Shankar, F., et al. 2017, *A&A*, **601**, A143
- Fletcher, T. J., Saintonge, A., Soares, P. S., & Pontzen, A. 2020, arXiv:2002.04959
- Fluetsch, A., Maiolino, R., Carniani, S., et al. 2019, *MNRAS*, **483**, 4586
- Freeman, P., Doe, S., & Siemiginowska, A. 2001, *Proc. SPIE*, **4477**, 76
- Fruscione, A., McDowell, J. C., Allen, G. E., et al. 2006, *Proc. SPIE*, **6270**, 62701V
- Gehrels, N., Chincarini, G., Giommi, P., et al. 2004, *ApJ*, **611**, 1005
- Georgakakis, A., Coil, A. L., Laird, E. S., et al. 2009, *MNRAS*, **397**, 623
- GILDAS Team 2013, GILDAS: Grenoble Image and Line Data Analysis Software, Astrophysics Source Code Library, ascl:1305.010
- Harris, C. R., Millman, K. J., van der Walt, S. J., et al. 2020, *Natur*, **585**, 357
- Heckman, T. M., & Best, P. N. 2014, *ARA&A*, **52**, 589
- Heckman, T. M., Blitz, L., Wilson, A. S., Armus, L., & Miley, G. K. 1989, *ApJ*, **342**, 735
- Hickox, R. C., Mullaney, J. R., Alexander, D. M., et al. 2014, *ApJ*, **782**, 9
- Hopkins, P. F., & Hernquist, L. 2006, *ApJS*, **166**, 1
- Hopkins, P. F., Hernquist, L., Cox, T. J., & Kereš, D. 2008, *ApJS*, **175**, 356
- Hunter, J. D. 2007, *CSE*, **9**, 90
- Ichikawa, K., Ricci, C., Ueda, Y., et al. 2017, *ApJ*, **835**, 74
- Ichikawa, K., Ricci, C., Ueda, Y., et al. 2019, *ApJ*, **870**, 31
- Janowiecki, S., Catinella, B., Cortese, L., et al. 2017, *MNRAS*, **466**, 4795
- Jarrett, T. H., Chester, T., Cutri, R., et al. 2000, *AJ*, **119**, 2498
- Jones, M. L., Hickox, R. C., Mutch, S. J., et al. 2019, *ApJ*, **881**, 110
- Kakkad, D., Mainieri, V., Brusa, M., et al. 2017, *MNRAS*, **468**, 4205
- Kauffmann, G., Li, C., Fu, J., et al. 2012, *MNRAS*, **422**, 997
- Kennicutt, R. C., & Evans, N. J. 2012, *ARA&A*, **50**, 531
- Kewley, L. J., Groves, B., Kauffmann, G., & Heckman, T. 2006, *MNRAS*, **372**, 961
- Kirkpatrick, A., Sharon, C., Keller, E., & Pope, A. 2019, *ApJ*, **879**, 41
- Kormendy, J., & Ho, L. C. 2013, *ARA&A*, **51**, 511
- Koss, M., Mushotzky, R., Baumgartner, W., et al. 2013, *ApJL*, **765**, L26
- Koss, M., Mushotzky, R., Treister, E., et al. 2011b, *ApJL*, **735**, L42
- Koss, M., Mushotzky, R., Treister, E., et al. 2012, *ApJ*, **746**, L22
- Koss, M., Mushotzky, R., Veilleux, S., et al. 2011a, *ApJ*, **739**, 57
- Koss, M., Mushotzky, R., Veilleux, S., & Winter, L. 2010, *ApJL*, **716**, L125
- Koss, M., Trakhtenbrot, B., Ricci, C., et al. 2017, *ApJ*, **850**, 74
- Koss, M. J., Assef, R., Baloković, M., et al. 2016, *ApJ*, **825**, 85
- Koss, M. J., Blecha, L., Bernhard, P., et al. 2018, *Natur*, **563**, 214
- Lamperti, I., Koss, M., Trakhtenbrot, B., et al. 2017, *MNRAS*, **467**, 540
- Lamperti, I., Saintonge, A., Koss, M., et al. 2019, arXiv:1912.01026
- Leroy, A. K., Walter, F., Bigiel, F., et al. 2009, *AJ*, **137**, 4670
- Leroy, A. K., Walter, F., Brinks, E., et al. 2008, *AJ*, **136**, 2782
- Lintott, C. J., Schawinski, K., Slosar, A., et al. 2008, *MNRAS*, **389**, 1179
- Lutz, D., Shimizu, T., Davies, R. I., et al. 2018, *A&A*, **609**, A9
- Mahoro, A., Pović, M., & Nkundabakura, P. 2017, *MNRAS*, **471**, 3226
- Maiolino, R., & Rieke, G. H. 1995, *ApJ*, **454**, 95
- Maiolino, R., Ruiz, M., Rieke, G. H., & Papadopoulos, P. 1997, *ApJ*, **485**, 552
- Malkan, M. A., Gorjian, V., & Tam, R. 1998, *ApJS*, **117**, 25
- Martini, P., & Pogge, R. W. 1999, *AJ*, **118**, 2646
- Martini, P., Regan, M. W., Mulchaey, J. S., & Pogge, R. W. 2003a, *ApJS*, **146**, 353
- Martini, P., Regan, M. W., Mulchaey, J. S., & Pogge, R. W. 2003b, *ApJ*, **589**, 774
- Mateos, S., Alonso-Herrero, A., Carrera, F. J., et al. 2012, *MNRAS*, **426**, 3271
- Meléndez, M., Mushotzky, R. F., Shimizu, T. T., Barger, A. J., & Cowie, L. L. 2014, *ApJ*, **794**, 152
- Monje, R. R., Blain, A. W., & Phillips, T. G. 2011, *ApJS*, **195**, 23
- Morganti, R., Frieswijk, W., Oonk, R. J. B., Oosterloo, T., & Tadhunter, C. 2013, *A&A*, **552**, L4
- Mullaney, J. R., Daddi, E., Béthermin, M., et al. 2012, *ApJL*, **753**, L30
- Mushotzky, R. F., Shimizu, T. T., Meléndez, M., & Koss, M. 2014, *ApJL*, **781**, L34
- Narayanan, D., Krumholz, M. R., Ostriker, E. C., & Hernquist, L. 2012, *MNRAS*, **421**, 3127
- Noll, S., Burgarella, D., Giovannoli, E., et al. 2009, *A&A*, **507**, 1793
- Nyland, K., Young, L. M., Wrobel, J. M., et al. 2016, *MNRAS*, **458**, 2221
- Oh, K., Sarzi, M., Schawinski, K., & Yi, S. K. 2011, *ApJS*, **195**, 13
- Oh, K., Yi, S. K., Schawinski, K., et al. 2015, *ApJS*, **219**, 1
- Papadopoulos, P. P., van der Werf, P. P., Xilouris, E. M., et al. 2012, *MNRAS*, **426**, 2601
- Perna, M., Sargent, M. T., Brusa, M., et al. 2018, *A&A*, **619**, A90
- Pety, J. 2005, in SF2A-2005: Semaine de l'Astrophysique Française, ed. F. Casoli et al. (Les Ulis: EDP Sciences), 721
- Popesso, P., Concas, A., Morselli, L., et al. 2019a, *MNRAS*, **483**, 3213
- Popesso, P., Morselli, L., Concas, A., et al. 2019b, *MNRAS*, **490**, 5285
- Pović, M., Sánchez-Portal, M., Pérez García, A. M., et al. 2012, *A&A*, **541**, A118
- Powell, M. C., Cappelluti, N., Urry, C. M., et al. 2018, *ApJ*, **858**, 110
- Renzini, A., & Peng, Y.-j. 2015, *ApJL*, **801**, L29
- Ricci, C., Trakhtenbrot, B., Koss, M. J., et al. 2017, *ApJS*, **233**, 17
- Ricci, C., Ueda, Y., Koss, M. J., et al. 2015, *ApJL*, **815**, L13
- Rigopoulou, D., Papadakis, I., Lawrence, A., & Ward, M. 1997, *A&A*, **327**, 493
- Robitaille, T., & Bressert, E. 2012, APLpy: Astronomical Plotting Library in Python, Astrophysics Source Code Library, ascl:1208.017
- Rojas, A. F., Sani, E., Gavignaud, I., et al. 2020, *MNRAS*, **491**, 5867
- Rosario, D. J., Burtcher, L., Davies, R. I., et al. 2018, *MNRAS*, **473**, 5658
- Rosario, D. J., Mendel, J. T., Ellison, S. L., Lutz, D., & Trump, J. R. 2016, *MNRAS*, **457**, 2703
- Rosas-Guevara, Y., Bower, R. G., Schaye, J., et al. 2016, *MNRAS*, **462**, 190
- Saintonge, A., Catinella, B., Cortese, L., et al. 2016, *MNRAS*, **462**, 1749
- Saintonge, A., Catinella, B., Tacconi, L. J., et al. 2017, *ApJS*, **233**, 22
- Saintonge, A., Kauffmann, G., Kramer, C., et al. 2011b, *MNRAS*, **415**, 32
- Saintonge, A., Kauffmann, G., Wang, J., et al. 2011a, *MNRAS*, **415**, 61
- Salim, S., Boquien, M., & Lee, J. C. 2018, *ApJ*, **859**, 11
- Sanders, D. B., Soifer, B. T., Elias, J. H., Neugebauer, G., & Matthews, K. 1988, *ApJL*, **328**, L35
- Sartori, L. F., Schawinski, K., Trakhtenbrot, B., et al. 2018, *MNRAS*, **476**, L34
- Schawinski, K., Koss, M., Berney, S., & Sartori, L. F. 2015, *MNRAS*, **451**, 2517
- Schawinski, K., Lintott, C. J., Thomas, D., et al. 2009, *ApJ*, **690**, 1672
- Schruba, A., Leroy, A. K., Walter, F., et al. 2011, *AJ*, **142**, 37
- Shangguan, J., Ho, L. C., Bauer, F. E., Wang, R., & Treister, E. 2019, arXiv:1912.00085
- Shimizu, T. T., Meléndez, M., Mushotzky, R. F., et al. 2016, *MNRAS*, **456**, 3335
- Shimizu, T. T., Mushotzky, R. F., Meléndez, M., et al. 2017, *MNRAS*, **466**, 3161
- Shimizu, T. T., Mushotzky, R. F., Meléndez, M., Koss, M., & Rosario, D. J. 2015, *MNRAS*, **452**, 1841
- Silverman, J. D., Mainieri, V., Lehmer, B. D., et al. 2008, *ApJ*, **675**, 1025
- Smith, K. L., Mushotzky, R. F., Koss, M., et al. 2020, *MNRAS*, **492**, 4216
- Solomon, P. M., Downes, D., Radford, S. J. E., & Barrett, J. W. 1997, *ApJ*, **478**, 144
- Strong, M., Pedlar, A., Aalto, S., et al. 2004, *MNRAS*, **353**, 1151
- Tacconi, L. J., Genzel, R., & Sternberg, A. 2020, arXiv:2003.06245
- Tiley, A. L., Bureau, M., Saintonge, A., et al. 2016, *MNRAS*, **461**, 3494
- Vassilev, V., Meledin, D., Lapkin, I., et al. 2008, *A&A*, **490**, 1157
- Veilleux, S., Kim, D.-C., Rupke, D. S. N., et al. 2009, *ApJ*, **701**, 587
- Veron-Cetty, M. P., & Veron, P. 2010, *A&A*, **518**, A10
- Vito, F., Maiolino, R., Santini, P., et al. 2014, *MNRAS*, **441**, 1059
- Wang, E., & Lilly, S. J. 2019, arXiv:1912.06523
- Wenger, M., Ochsenbein, F., Egret, D., et al. 2000, *A&AS*, **143**, 9
- Wright, E. L., Eisenhardt, P. R. M., Mainzer, A. K., et al. 2010, *AJ*, **140**, 1868
- Yamada, T. 1994, *ApJ*, **423**, L27
- Yang, G., Brandt, W. N., Darvish, B., et al. 2018, *MNRAS*, **480**, 1022
- Yang, G., Chen, C. T. J., Vito, F., et al. 2017, *ApJ*, **842**, 72
- Yates, R. M., Kauffmann, G., & Guo, Q. 2012, *MNRAS*, **422**, 215
- Young, L. M., Bureau, M., Davis, T. A., et al. 2011, *MNRAS*, **414**, 940